GEOLOGICA CARPATHICA, OCTOBER 2017, 68, 5, 445–463 doi: 10.1515/geoca-2017-0029

Geochemical characteristics and conditions of formation of the Chah-Bazargan peraluminous granitic patches, ShahrBabak, Iran

ABDOLNASER FAZLNIA

Department of Geology, Urmia University, 57153-165 Urmia, Islamic Republic of Iran; a.fazlnia@urmia.ac.ir, nfazlnia@yahoo.com

(Manuscript received November 27, 2016; accepted in revised form June 9, 2017)

Abstract: Xenoliths of garnet–biotite–kyanite schist from the Qori metamorphic complex (southern part of the Sanandaj–Sirjan zone, northeast Neyriz, Zagros orogen in Iran) in the 173.0±1.6 Ma Chah-Bazargan leuco-quartz diorite intrusion were studied. This intrusion caused these schist xenoliths to be metamorphosed to the pyroxene hornfels facies (approximately 4.5±1.0 kbar and 760±35 °C), converting them to diatexite migmatite as a result of partial melting of the xenoliths. These melts are granites in composition. Melt volumes of 20 to 30 vol. % were calculated for small patches of the peraluminous granites. It is possible that anatectic melting affected only the leucosome, such that melting was more than 20 to 30 vol. %. It is possible that a large amount of melt was not extracted due to balanced in situ crystallization, the adhesion force between melt and crystal (restite), and high viscosity of the leucosome. The Chah-Bazargan peraluminous granites are depleted in trace elements such as REEs, HFSE (Ti, Zr, Ta, Nb, Th, U, Hf, Y), Ba, Pb, and Sr. These elements are largely insensitive to source enrichment, but sensitive to the amounts of main and accessory minerals. These elements were hosted by minerals such as garnet, biotite, muscovite, K-feldspar, plagioclase, ilmenite, apatite, monazite, and zircon in the source (diatexitic migmatitic xenoliths).

Keywords: geochemistry, partial melting of xenoliths, peraluminous granitic patches, Jurassic.

Introduction

Migmatites provide examples of nascent granites, but detailed studies often reveal that their leucosomes are the locations of melt depletion rather than crystallization, or at best status, crystal-melt mixes (e.g., Mehnert 1968; Ashworth 1985; Sawyer 2008a, b). In some instances, segregated and homogeneous granites within migmatitic terrains of the mid-crust can be related to specific sedimentary sources and melting reactions as exemplified by Himalayan leucogranites, (Harris et al. 1995) because the melts have not migrated far from their sources. However, some recent studies (Carvalho et al. 2016) have shown that leucosome can also be connected to the granite melt far from their sources.

The processes of melt formation and extraction and crustal source composition strongly influence the chemistry of granitic melts. The melts have very low levels of trace elements such as Rb, Zr, Th, U, and Y where melt-residue separation is very efficient, as in leucosomes of stromatic migmatites (metatexites), (Bea 1996a; Sawyer 1996; Sheppard et al. 2003). The depleted nature of the melts is typically ascribed to disequilibrium melting where the rate of melt extraction exceeds the rate at which accessory phases dissolve (Sawyer 1991), or to shielding of accessory phases by inclusion in mafic minerals during melt formation and extraction (Bea 1996b). Metatexite is a migmatite heterogeneous at the outcrop scale and coherent pre-partial melting structures are widely preserved in the paleosome (where the microstructure appears unchanged) and possibly in the melanosome (residuum) part of the neosome where the fraction of melt was low (Makrygina 1977; Bucher & Grapes 2011).

Diatexite is a migmatite in which neosome is dominant and melt was pervasively distributed throughout. Pre-partial-melting structures are absent from the neosome and commonly replaced by syn-anatectic flow structures (e.g., magmatic or submagmatic foliations, schlieren), or isotropic neosome. Neosomes are diverse, reflecting a large range in the fraction of melt, and they can range from predominantly leucocratic to predominantly mesocratic (e.g., unsegregated melt and residuum) to predominantly melanocratic. Palaeosome occurs as rafts and schollen, but may be absent (Sawyer 2008b). Diatexite migmatites represent high degrees of partial melting, typically in the highest grade parts of migmatite terrains (Mehnert 1968; Sawyer 2008b), and contain large and variable proportions of restite. Diatexites are more homogenous than metatexites, because there is considerable movement of the melt fraction from one place to another within the diatexite migmatites (Sawyer 2008b).

Terms appropriate to metatexite migmatites are patch, dilation, net, and stromatic structures. These structures are formed at the very onset of partial melting of the source. At the onset of partial melting, the fraction of melt in a migmatite is very small of course and this precludes the development of an eye-catching morphology. Nevertheless, it is very important to identify these migmatites because their appearance defines the lower-grade limit to migmatite terrains. Partial

melting in a rock typically starts at a few dispersed sites where the conditions are optimal for the melt-producing reaction to proceed (Raymond 2007; Sawyer 2008a,b).

Terms appropriate to diatexite migmatites are nebulitic, schollen, and schlieren structures. As the fraction of melt and neosome creation increase in a metatexite migmatite, the pre-anatectic structures in the migmatite are progressively destroyed. However, new micro- and macrostructures are produced during anatexis and become evident in the neosome. The precise morphology that develops depends on whether deformation occurred or the original distribution of fertile rock types (Raymond 2007; Sawyer 2008a,b).

This study presents field, petrographic and geochemical data and uses them to reconstruct the partial melting history of migmatitic metapelitic xenoliths from Chah-Bazargan batholith, in the southern part of the Sanandaj–Sirjan zone, northeast Neyriz, Zagros orogen in Iran. This study demonstrates the relationships among the migmatites, leucogranites, and pegmatites, and shows that these rocks formed in the middle crust as a consequence of advective heating by quartz dioritic magma.

Geological setting

Southern Iran can be divided into a set of three parallel NW–SE trending tectonic zones including: the Zagros Fold-Thrust Belt, the Sanandaj–Sirjan Zone, and the Tertiary–Quaternary Urumieh–Dokhtar magmatic arc (Alavi 1994; Mouthereau et al. 2012; Mohajjel & Fergusson 2014; Hassanzadeh & Wernicke 2016), (Fig. 1). The Zagros is the largest mountain belt and the most active collisional orogen associated with Arabia/Eurasia convergence. It belongs to the Alpine–Himalayan orogenic system that resulted from closure of the Neotethys Ocean during the Cenozoic (Alavi 1994; McQuarrie et al. 2003; Mouthereau et al. 2012; Hassanzadeh & Wernicke 2016). The tectonic history of these zones as part of the Tethyan region has been summarized by many authors (e.g., Berberian & King 1981; Alavi 1994; Omrani et al. 2008; Khadivi et al. 2012; Mouthereau et al. 2012; Fazlnia et al. 2013; Mohajjel & Fergusson 2014; Shafaii Moghadam et al. 2014; Hassanzadeh & Wernicke 2016). The Sanandaj–Sirjan zone juxtaposed various metamorphic and magmatic rocks that mostly formed in the Mesozoic era. It is believed that the zone mostly consists of arc-related calc-alkaline granitoid, gabbro and some volcanic rocks along with amphibolite and kyanite-garnet schist formed during the subduction of Neotethys beneath the Iranian plate (Berberian & King 1981; Alavi 1994; Mouthereau et al. 2012). During the Palaeozoic period, the Sanandaj–Sirjan zone was a part of northeast Gondwanaland separated from the Eurasian plate by the Palaeo-Tethys Ocean (Golonka 2004; Mouthereau et al. 2012; Fazlnia & Alizade 2013). A north-dipping subduction system developed along the Palaeotethys margin (Golonka 2004). This subduction system played a significant role in driving the Late Palaeozoic and Early Mesozoic movement of plates in this area.

From early Permian to early Triassic times, the Sanandaj–Sirjan zone had been situated along the southern margin of the Eurasian plate and separated from northern Gondwanaland by the Neotethyan Ocean (Mouthereau et al. 2012). During Late Triassic–Early Jurassic times, several microplates were sutured to the Eurasian margin, closing the Palaeotethys Ocean (Golonka 2004). A north-dipping Neotethys subduction zone beneath the Sanandaj–Sirjan plate was started approximately in the Bajocian (Middle Jurassic; Golonka 2004; Yousefirad 2011; Fazlnia et al. 2013; Sheikholeslami 2015; Hassanzadeh & Wernicke 2016). The formation and evolution of the Neotethys started from Late Palaeozoic times (Hassanzadeh & Wernicke 2016). Therefore, the tectonic regime between the Arabian margin and Sanandaj–Sirjan plate altered from passive to convergent (Ricou 1994). During the Mesozoic, the oceanic crust of the Neotethys was subducted beneath the Eurasian plate (Golonka 2004; Molinaro et al. 2005; Agard et al. 2011; Yousefirad 2011; Mouthereau et al. 2012; Karimi et al. 2012; Fazlnia et al. 2013; Mohajjel & Fergusson 2014; Sheikholeslami 2015), and the Sanandaj–Sirjan zone occupied the position of a magmatic arc (Berberian & Berberian 1981; Agard et al. 2005; Agard et al. 2011; Karimi et al. 2012; Mouthereau et al. 2012; Fazlnia et al. 2013; Chiu et al. 2013; Mohajjel & Fergusson 2014; Akbari et al. 2016; Hassanzadeh & Wernicke 2016). Subduction and arc magmatism began in latest Triassic/Early Jurassic time, culminating at ~170 Ma (Hassanzadeh & Wernicke 2016). The final closure of the Neotethys and the collision of the Arabian and Eurasian plates took place during the Tertiary period (Berberian & Berberian 1981; Alavi 1994; Golonka 2004; Molinaro et al. 2005; Omrani et al. 2008; Agard et al. 2011; Mouthereau 2011; Yousefirad 2011; Khadivi et al. 2012; Mouthereau et al. 2012; Mohajjel & Fergusson 2014; Sheikholeslami 2015). Based on Hassanzadeh & Wernicke (2016) the collision took place during the mid-Tertiary. During the same period, the Zagros Fold-Thrust Belt formed as part of the Alpine–Himalayan mountain chain, extending about 2000 km from eastern Turkey to the Oman line in southern Iran (Berberian & King 1981; Alavi 1994; Agard et al. 2005; Omrani et al. 2008; Agard et al. 2011; Mouthereau 2011; Mouthereau et al. 2012; Mohajjel & Fergusson 2014; Sheikholeslami 2015). The Chah-Bazargan intrusion is located in northeast Neyriz which is a part of the south Sanandaj–Sirjan zone.

There are several outcrops of intrusion-bordering migmatites in the middle part of the Sanandaj–Sirjan zone. The migmatites occurred around the Alvand aureole near Hamadan (Fig. 1), western Iran (Saki et al. 2012). They suggested that regional metamorphism, granitic magmatism (Alvand pluton), and contact metamorphism reflect arc construction and collision during subduction of a Neotethyan seaway and subsequent Late Cretaceous–early Tertiary oblique collision of Afro-Arabia (Gondwana) with the Iranian microcontinent. The Chah-Bazargan intrusion and migmatitic xenoliths within the intrusion are like those in the Alvand aureole near Hamadan (Fig. 1).

Rocks of the Chah-Bazargan intrusion are composed of quartz-diorite (Table S1) along with small patches of gabbroic

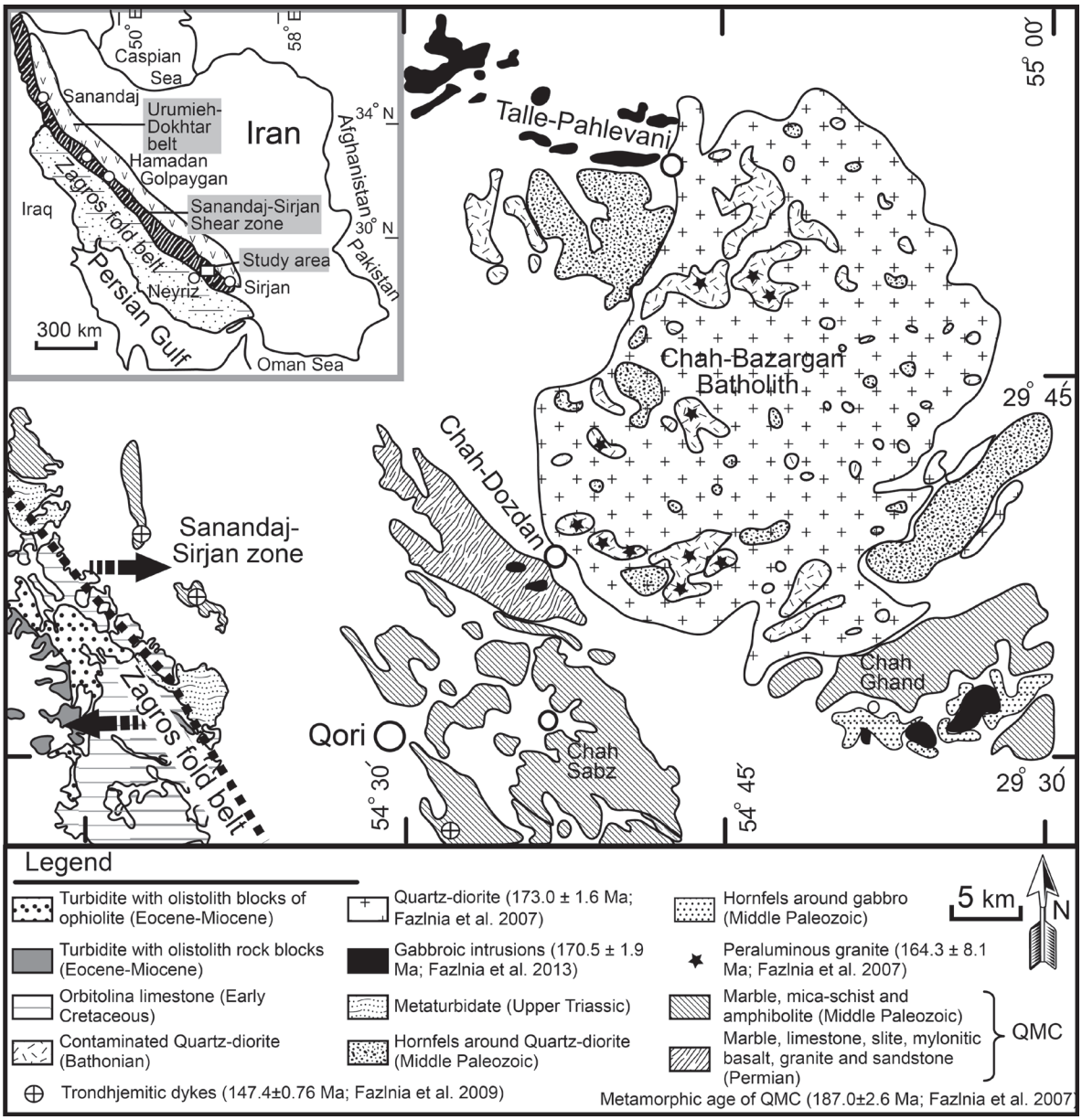

Fig. 1. Simplified geological map of north-eastern Neyriz (modified after Sabzehei et al. 1992). More information about sample locations are present in Table S2.

intrusions (Fazlnia et al. 2013), migmatitic xenoliths (several centimetres to several tens of metres in size), tourmaline-bearing pegmatites and peraluminous garnet- and cordierite-bearing granites (metre to several tens of metres in size; Fazlnia et al. 2007; Fig. 1; Table S1). The initial Chah-Bazargan intrusion is mostly composed of plagioclase (90–95 vol. %) and quartz (5–10 vol. %), as granular and cumulative textures, along with accessory minerals (1–2 vol. %) such as clinopyroxene and titanite. This intrusion crystallized at 173.0±1.6 Ma (Fazlnia et al. 2007) into medium to high grade parts of the arc-related Qori Barrovian-type metamorphic complex (QMC; Fazlnia et al. 2013; Sheikholeslami 2015), which primarily consists of meta-basites (actinolite schist to garnet amphibolite) and meta-pelitic (biotite to garnet–kyanite–biotite schist), interspersed with meta-psammitic, meta-ultramafic (olivine–orthopyroxene–spinel–hornblende schist), and marbles layers (Table S1). The Talle-Pahlevani gabbroic intrusions (Fig. 1) infiltrated into the Qori metamorphic complex as a result of Neotethys subduction beneath central Iran 170.5±1.9 Ma (Fazlnia et al. 2009; Sheikholeslami 2015). Therefore, there is a possibility that the Chah-Bazargan quartz-dioritic and Talle-Pahlevani gabbroic intrusions (Table S1) were formed of the same magma. This is highlighted by the very similar spider diagram patterns (Fazlnia et al. 2009, 2013) of the intrusive rocks. Consequently, it is probable that the Chah-Bazargan quartz-diorites are most likely cumulates of a basaltic to andesitic magma and the Talle-Pahlevani gabbroic intrusions were

formed at the base of the Chah-Bazargan quartz-dioritic intrusions.

The Barrovian-type metamorphic event in the QMC occurred ca. 187.0±2.6 Ma (Fazlnia et al. 2007, 2009; Sheikholeslami 2015). Regional metamorphic mineral assemblages in meta-pelites mainly consist of Ky+St+Grt+Bt+Ms+Pl+Qtz and Ky+Grt+Bt+Pl+Qtz±Ms. Some outcrops of sedimentary and low grade metasedimentary rocks can be found among the high grade metamorphic rocks due to late stage shearing of the Zagros fold belt (Berberian & King 1981; Sabzehei et al. 1992; Saki et al. 2012; Sheikholeslami 2015). All rock types are sheared strongly and thrust as imbricate slices over the Neyriz ophiolite (Berberian & King 1981; Sabzehei et al. 1992; Alavi 1994; Babaei et al. 2001; Mohajjel et al. 2003; Sheikholeslami et al. 2008; Fazlnia et al. 2009; Sarkarinejad et al. 2009; Sheikholeslami 2015). The peak pressure and temperature for the Qori metamorphic complex (Fig. 1) have been estimated to be 9.2±1.2 kbar and 705±40 °C resulting from crustal thickening during the Early Cimmerian orogeny between 187 and 180 Ma (Fazlnia et al. 2007, 2009). This event occurred as a result of the beginning of Neotethys subduction beneath central Iran (Fazlnia et al. 2013; Sheikholeslami 2015). The studied rock types are related to this event.

The host rock (medium to high grade parts of the QMC) was disrupted as the primary magma (Chah-Bazargan gabbroic intrusions) was injected. Xenoliths of the host rock underwent high temperature contact metamorphism. Some meta-pelitic xenoliths were completely assimilated by magma and converted the mineral assemblage of the surrounding Chah-Bazargan quartz-diorite to biotite granodiorite-tonalite intrusion (Fazlnia et al. 2007). Small peraluminous patches of two-mica granite and tourmaline-bearing pegmatites occur in association with aggregations of meta-pelitic xenoliths within the intrusion (Fazlnia et al. 2007). Previous studies (Sabzehei et al. 1992; Jamshidi 2003) did not report any migmatitic xenoliths and peraluminous two-mica granite in the intrusion. Sheikholeslami et al. (2003) concluded that the Chah-Bazargan intrusion was emplaced at ca. 160±10 Ma on the basis of biotite K–Ar ages. Fazlnia et al. (2007) demonstrate that the crystallization of the primary quartz-dioritic magma and peraluminous granite occurred 173.0±1.6 Ma and 164.3±8.1 Ma, respectively, and melting recorded by the migmatitic xenoliths 167±3.1 Ma considering the zircon SHRIMP U–Pb ages.

Additionally, the western edge of the QMC underwent another Barrovian-type metamorphism at 147.4±0.76 Ma as a result of crustal thickening during the initiation of the Neotethyan mid-ocean ridge subduction beneath central Iran. The metamorphic circumstance generated garnet amphibolites occurred at pressures and temperatures between 7.5 and 9.5 kbar (at depth of 28 to 36 km) and 680 and 720 °C, respectively, based on the Grt–Hbl and Hbl–Pl thermometers and Grt–Hbl–Pl–Qtz barometer (Fazlnia et al. 2009; also see Sheikholeslami 2015). There is no evidence for the occurrence of this metamorphism in the eastern part of the study area (e.g., Chah-Bazargan, Chah-Dozdan, and Chah-Sabz).

Field and petrographic observations

Quartz diorites are leucocratic and contain xenoliths of meta-pelitic migmatite. These xenoliths are between several centimetres and several decimetres in diameter. The magmatic rocks contain up to 93 % plagioclase, with minor quartz, apatite, epidote, titanite, ilmenite, and zircon. Zircon grains obtained from two samples have prismatic euhedral shapes and probably crystallized from quartz dioritic magma (Fazlnia et al. 2007). The initial texture of quartz-diorites was granular, but this early magmatic texture has been overprinted to mylonite as a result of shearing during the Neotethys closing in the Late Cenozoic (Mohajjel et al. 2003; Golonka 2004; Davoudian et al. 2008). The accessory minerals mentioned are euhedral and form the matrix along with quartz, suggesting magmatic crystallization in small pegmatitic and coarse-grained patches.

There are five types of xenoliths: (a) cognate enclaves: fine-grained inclusions of quartz diorite, (b) basaltic andesite to andesite, (c) meta-pelite, (d) meta-basite, and (e) xenoliths with large grains of quartz which contain abundant inclusions of orthopyroxene, clinopyroxene, two types of amphibole, plagioclase, biotite, muscovite and tourmaline. Here we describe only the meta-pelitic xenoliths derived from the country rocks, because they are plentiful and played a significant role in contaminating the quartz dioritic magma and also producing peraluminous granites and tourmaline pegmatites. It should be noted that many of the xenoliths are migmatite.

Many meta-pelitic xenoliths throughout Chah-Bazargan batholith underwent high-grade contact metamorphism within the batholith. Some of them have abundant bands, pods and patches of leucocratic quartzo-feldspathic leucosome that is interpreted as former melt visible in hand specimens (Fig. 2) and microscopic scale (Fig. 3a,b). Segregation of the melt from the residual phases (melanosome; Fig. 2a–c,e) of meta-pelitic (migmatitic) xenoliths such as cordierite, biotite and garnet (in some xenolithic aggregations) have formed small peraluminous granite patches in the intrusion. The small dark patches are fragments of melanosome just to the right of the mesosome (a mixture of melt and the refractory and relic parts; Fig. 2b), up and center of the Fig. 2e.

Metapelitic xenoliths in the Chah-Bazargan batholith can be subdivided into stromatic migmatites with mesosomes and leucosomes (Fig. 2a,c), and nebulitic migmatites (Fig. 2b, d–e). Stromatic migmatites represent the lower-grade migmatites, extensively similar to metatexites as defined and described by Brown (1979; also see geochemistry section). Stromatic migmatites consist of small-scale (several mm to several cm) alternating layers of neosome and mesosome. The pre-migmatisation fabric is well preserved within the paleosome (Fig. 2a,c) and the ratio of leucosome to melanosome in the neosome may vary. The relationship between the melanosomes and leucosomes of the stromatic migmatites is mostly gradational (Fig. 2a,c).

Nebulitic migmatites (Fig. 2b,d) are similar to the diatexites (there are schlieren in the Fig. 2b,e) of Mehnert (1968), Brown

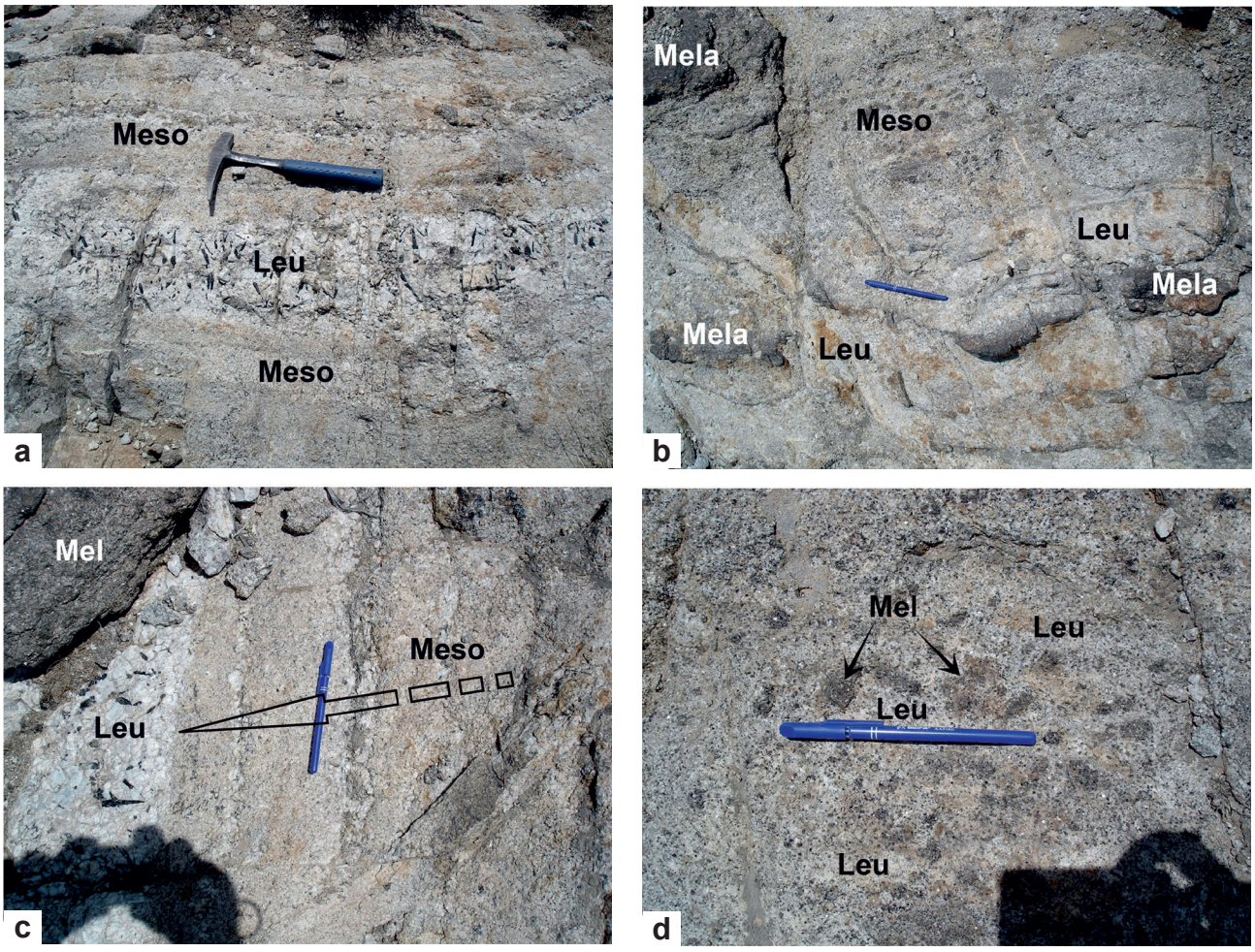

Fig. 2. Photos of migmatitic xenoliths. **a** — Outcrop of stromatic-structured metatexite migmatites with mesosomes and leucosomes; **b** — Morphology of nebulitic-structured diatexite migmatites. This is a mafic schlieren oriented parallel to the foliation in the upper right; **c** — Outcrop of stromatic-structured metatexite migmatites. The relationship between the mesosomes and leucosomes is gradational; **d** — Diatexite migmatites with a simple morphology. They are characteristic of the highest grade parts of xenoliths where the proportion of neosome is very high. Schlierens (melanosome) are dispersed throughout the leucosome.; **e** — The individual melanosome (mafic schlieren) in nebolitic-structured diatexite migmatite.

(1979), and Sawyer (2008b). They usually represent higher-grade migmatites. Nebulitic migmatites (migmatite with diffuse relics of pre-existing rocks or rock structures) contain irregular islets of neosome dispersed in the paleosome, the limits between these two are blurred and irregular. Typically, they are located close to small patches of peraluminous granite in the Chah-Bazargan intrusion. Leucosomes occur mostly as concordant veins with diffuse and irregular borders towards the melanocratic rock portions. There is considerable variation in the proportion of mafic relative to leucocratic material, usually the mafic material forms ample mafic schlieren oriented parallel to the foliation (Fig. 2b). The relationship between the nebulitic migmatites and small peraluminous granitic patches is mostly gradational. Diatexite migmatites with

a mixed morphology of melanosome and leucosome (Fig. 2d) are characteristic of the highest grade parts of the xenoliths where the proportion of neosome is very high (see also Sawyer (2008b) for more discussion).

K-feldspar in the meta-pelitic (migmatitic) xenoliths occurs as small to large irregular to regular perthitic crystals (0.2–5 mm), which shows eutectic intergrowth with quartz. Plagioclase occurs as a large and euhedral mineral (Fig. 3) with zoning (Fig. 3c,e; mineral chemistry section shows plagioclase composition). Cordierite is commonly subhedral to euhedral with inclusions of spinel, quartz, and biotite in the same grain (Fig. 3d,e,i). Garnet in meta-pelitic xenoliths was either consumed or present as relict phases in quartz and plagioclase (Fig. 3b,e) as a result of partial melting in meta-pelitic (migmatitic) xenoliths. Sillimanite is found as both fibrolite mats and prismatic grains (Fig. 3d) during contact metamorphism in the meta-pelitic xenoliths. The former is present as a retrograde phase along with biotite, poikilobastic plagioclase and ilmenite. The latter is present in prograde mineral assemblages (Table S2) along with garnet, spinel, cordierite and K-feldspar (Fig. 3d) during contact metamorphism; it is also presented as a result of a replacement process in late-stage muscovite (Fig. 3h). Muscovite in many meta-pelitic xenoliths is only present within quartzo-feldspathic veins (Fig. 3f), suggesting that it may have been formed during the late stage of crystallization of the melt (restite-melt back reaction), but in the other parts it is probably a retrograde phase around cordierite and/or sillimanite (Fig. 3h). Spinel occurs together with prograde mineral assemblages in the matrix (Table S2; Fig. 3g) or as an inclusion phase in cordierite (Fig. 3f), but spinel and quartz are not in contact together. Some metapelitic xenoliths that have up to 80 % cordierite, biotite, and K-feldspar have corundum in the matrix (Fig. 3j) but no quartz. Some meta-pelitic xenoliths have ~75 % cordierite, suggesting that they are residues after partial melting or reflect an unusual starting bulk composition.

Small patches of peraluminous granite (one metre to several tens metres across) that occur as sharp lenses and tourmaline pegmatites (tens centimetres to several metres across and tens of metres in length; average grain size is 1–50 mm), veins or sheets are located adjacent to diatexitic xenoliths. Peraluminous granites have two kinds of mineral assemblages (average grain size is 0.2–5 mm): (a) Kfs–Pl–Qtz–Bt–Ms–Crd–Sil–Tur, and (b) Kfs–Pl–Qtz–Bt–Ms–Grt–Sil–Tur±Crd (Tables S1, S2; mineral abbreviations after Kretz (1983)). K-feldspar, quartz and plagioclase are abundant minerals in this rock type. Mineralogically and texturally, they are similar to quartzo-feldspathic melt veins within metapelitic xenoliths (leucosome; Fig. 2). Texturally, all peraluminous granites are granular and granophyric with perthitic alkali feldspar suggesting that quartz, K-feldspar and albite crystallized as eutectic intergrowths. Cordierite and garnet occur as porphyroblastic xenocrysts similar to the diatexitic xenoliths. Garnet is subhedral and generally rounded without inclusions. Cordierite is subhedral with many inclusions of quartz, spinel, biotite, muscovite, and tourmaline. Sillimanite occurs as prismatic inclusions in muscovite, whereas muscovite and other minerals are presented in a granular texture. This suggests that sillimanite is xenocrystic from the metapelitic xenoliths whereas muscovite is the result of late magmatic crystallization.

Analytical methods

All microprobe analyses were performed with a JEOL JXA 8900 microprobe at the University of Kiel, Germany. For the analyses of major phases we used a 15 or 20 nA probe current at an accelerating potential of 15 kV. Selected standard names of the oxides SiO_2, MnO, CaO, MgO, TiO_2, Al_2O_3, FeO, Na_2O, and K_2O for all minerals are wolMAC, teph, wolMAC, foMAC, rt_st8, crn657s, fay85276, ano133868, and mic143966, respectively. Standard deviations (S.D. (%)) of Si, Mn, Ca, Mg, Ti, Al, Fe, Na, and K for all analysed points are 0.12, 0.26, 0.15, 0.14, 0.12, 0.09, 0.26, 0.4, and 0.23, respectively. Composition of perthitic K-feldspar was calculated by analyses of BSE images and point-counting of the perthite. Major-element mineral compositions in selected samples of the Chah-Bazargan batholith are listed in Table S3. Analyses of coexisting minerals were obtained for Sil–Crd–Grt- and Crd–Kfs–Grt–Sil-bearing xenoliths, peraluminous granites, host rocks (quartz-diorite), and contaminated host rocks.

Table 1 lists the chemical compositions of 20 representative samples obtained by XRF (X-ray florescence instrument; Philips PW 1480) at the University of Kiel, Germany. Major elements were measured using fusion beads. H_2O^- of samples (moisture) was determined by heating powders at 110 °C for 2 hours and calculated from the decrease in powder weights. LOI (loss on ignition) of samples was determined by heating powders of the samples at 1000 °C for 2 hours. The decrement

Fig. 3. Photos of migmatitic metapelitic xenoliths. **a** — (XPL light) and **b** — (PPL light) high-grade contact metamorphism (nebulitic-structured diatexite migmatite) along with bands, pods and patches of leucocratic quartzo-feldspathic melt (leucosome). Biotite shows a poikiloblastic texture, suggesting dehydration melting of biotite; **c** — Plagioclase with oscillatory zoning surrounded the cordierite and biotite suggesting the presence of melt in the migmatitic xenoliths (XPL light); **d** — Prismatic sillimanite along with biotite+cordierite+plagioclase+K-feldspar+quartz in the migmatitic xenoliths (PPL light). Spinel is present within cordierite; **e** — Plagioclase with oscillatory zoning surrounding absorbed garnet and biotite manifest that melt is present in the migmatitic xenoliths (XPL light); **f** , **g** — Presence of spinel within cordierite (XPL light) and in matrix (PPL light), respectively, suggests high-grade contact metamorphism in the migmatitic xenoliths; **h** — Presence of late-stage muscovite around sillimanite; **i** — Picture of leucosome from nebulitic-structured diatexite migmatite. There is late-stage muscovite around biotite; **j** — Presence of corundum in the matrix. This sample contains cordierite, biotite, and K-feldspar up to 80 %. Abbreviations are after Kretz (1983).

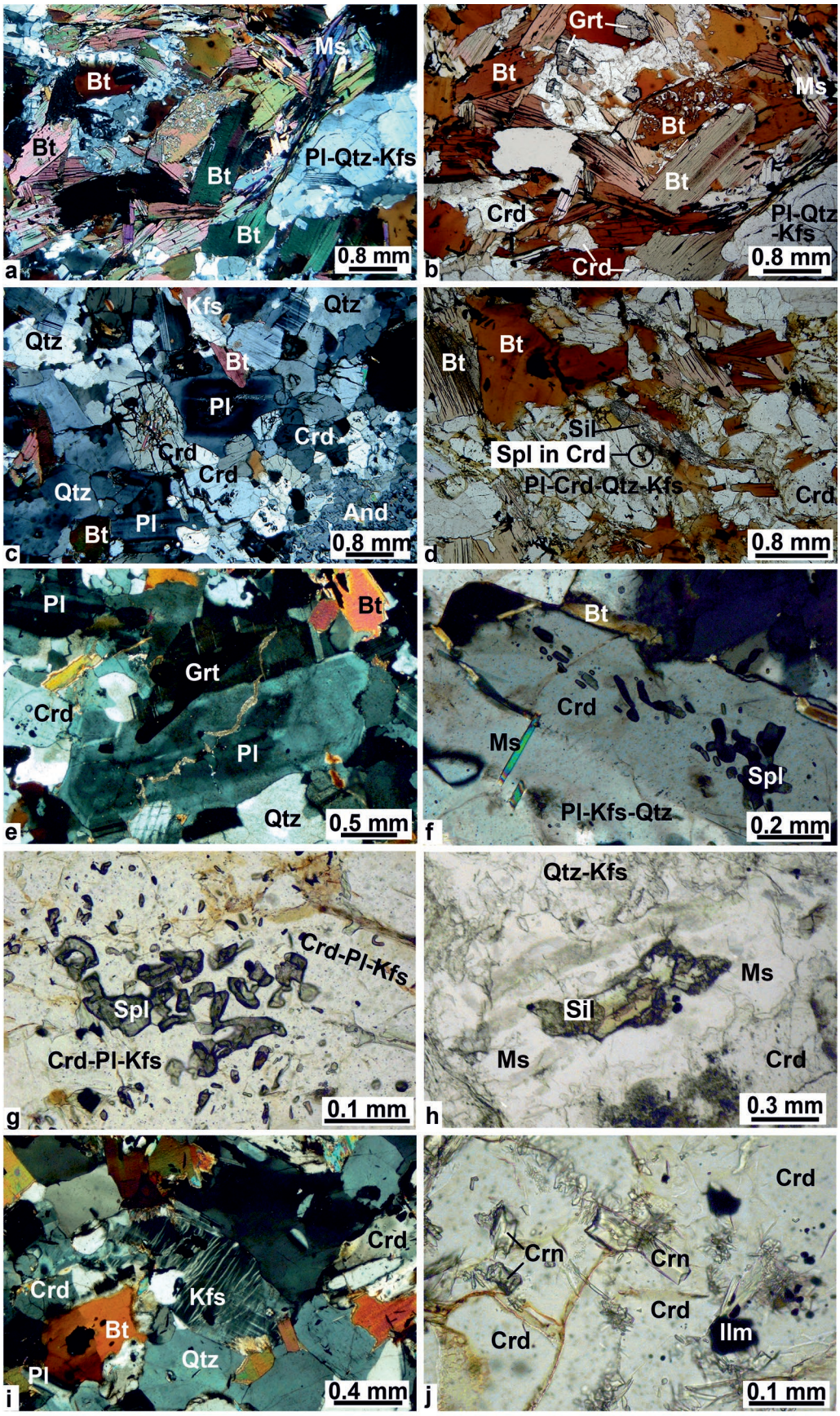
Ms
Bt
Bt
Pl-Qtz-Kfs
Bt
Bt
0.8 mm
a
Grt
Bt
Ms
Bt
Bt
Crd
Pl-Qtz
-Kfs
Crd
0.8 mm
b
Kfs
Qtz
Qtz
Bt
Pl
Crd
Crd
Crd
Qtz
And
Bt
Pl
0.8 mm
c
Bt
Bt
Sil
Spl in Crd
Pl-Crd-Qtz-Kfs
Crd
0.8 mm
d
Pl
Bt
Grt
Crd
Pl
Qtz
0.5 mm
e
Bt
Crd
Ms
Spl
Pl-Kfs-Qtz
0.2 mm
f
Crd-Pl-Kfs
Spl
Crd-Pl-Kfs
0.1 mm
g
Qtz-Kfs
Ms
Sil
Ms
Crd
0.3 mm
h
Crd
Crd
Kfs
Bt
Qtz
Pl
0.4 mm
i
Crd
Crn
Crn
Crd
Crd
Ilm
0.1 mm
j

Sample		140-1	187	190-B	189-E	260	264	272	181-E	182-E2	183-E1	188-E1	189-E3	190-E1	191-E5	192-E2	193-E3	111-c	114-a	220	221	Average	Average	Average
Rock type		P-g	P-g	P-g	P-g	P-g	P-g	P-g	Xeno	Xeno	Xeno	Xeno	Xeno	Xeno	Xeno	Xeno	Xeno	Pelite	Pelite	Pelite	Pelite	of Granite	migmatite Xenolith	metapelite & Xenolith
	MDL	Grt	Grt	Grt	Grt	Crd	Crd	Crd	Mig	Mig	Mig													
	wt. %	Kiel	Kiel	Kiel	Kiel	Kiel	Kiel	Kiel	Kiel	Kiel	Kiel	Kiel	Kiel	Kiel	Kiel	Kiel	Kiel	Kiel	Kiel	Kiel	Kiel			
SiO_2	0.01	74.12	73.91	73.58	74.45	74.29	75.30	75.24	43.39	62.68	57.22	66.82	64.25	59.22	63.05	65.11	60.22	59.04	64.16	58.2	60.64	74.35	54.43	62.07
Al_2O_3	0.01	13.85	14.03	14.18	13.85	13.65	13.18	13.11	26.77	17.71	20.12	16.41	16.65	18.83	17.13	16.36	17.35	19.41	16.96	19.48	16.09	13.73	21.53	17.47
TiO_2	0.01	0.06	0.05	0.05	0.09	0.07	0.09	0.08	2.14	0.92	1.17	0.29	0.58	0.39	0.85	0.75	0.87	0.81	0.74	0.88	0.85	0.07	1.41	0.70
MgO	0.01	0.14	0.11	0.13	0.27	0.31	0.26	0.28	5.17	2.07	4.87	1.90	2.15	3.75	2.55	2.01	3.55	1.87	3.56	3.46	3.65	0.20	4.04	2.85
FeO*	0.04	1.28	1.10	1.38	1.21	1.20	1.24	1.23	15.74	6.92	10.53	5.84	4.85	6.27	6.33	5.88	7.49	5.80	5.65	6.96	7.50	1.24	11.06	6.26
CaO	0.01	0.65	0.72	0.59	0.71	0.66	0.63	0.56	0.84	1.34	1.21	2.44	3.05	1.59	2.21	2.45	1.22	0.64	0.74	0.52	0.75	0.65	1.13	1.56
P_2O_5	0.01	0.10	0.11	0.12	0.11	0.11	0.12	0.12	0.03	0.15	0.08	0.05	0.12	0.13	0.09	0.11	0.19	0.17	0.15	0.21	0.21	0.11	0.09	0.14
Na_2O	0.01	2.04	1.82	2.32	2.95	2.73	2.87	2.83	0.79	1.79	0.84	2.16	2.88	2.44	1.73	1.81	1.94	0.43	1.58	1.71	1.93	2.45	1.14	1.86
K_2O	0.01	5.95	6.20	6.10	5.05	5.21	5.04	5.10	1.76	3.90	1.55	1.70	2.55	4.12	3.87	2.94	4.18	6.81	2.33	3.75	4.09	5.59	2.40	3.63
MnO	0.01	0.06	0.07	0.06	0.04	0.05	0.05	0.04	0.40	0.11	0.34	0.18	0.24	0.20	0.24	0.18	0.17	0.27	0.06	0.08	0.16	0.05	0.28	0.18
Total		98.25	98.16	98.51	98.77	98.28	98.81	98.64	97.21	97.75	97.93	97.86	97.32	96.94	98.05	97.60	97.18	95.25	95.93	95.25	95.87	98.47	97.63	96.73
LOI		1.25	1.08	0.75	0.91	1.12	0.86	0.84	2.02	2.07	1.81	2.03	2.32	1.65	1.48	1.88	1.68	3.45	3.43	3.52	2.4	0.98	1.97	2.38
CIPW norm																								
Qtz		37.09	37.26	34.79	35.37	35.91	36.91	36.98	10.74	26.62	28.56	35.01	24.51	15.51	25.04	30.89	19.82	22.33	35.36	23.00	21.54	36.275	21.97	25.3
Or		35.16	36.64	36.05	29.84	30.79	29.78	30.14	10.40	23.05	9.16	10.05	15.07	24.35	22.87	17.37	24.70	40.24	13.77	22.14	24.17	33.035	14.20	21.45
Ab		17.26	15.40	19.63	24.96	23.1	24.29	23.95	6.68	15.15	7.11	18.28	24.37	20.65	14.64	15.32	16.42	3.64	13.37	14.47	16.33	20.775	9.65	15.74
An		2.57	2.85	2.14	2.80	2.56	2.34	1.99	3.97	5.67	5.48	11.78	14.35	7.04	10.38	11.44	4.81	2.06	2.69	1.21	2.35	2.45	5.04	6.82
Crn		3.11	3.28	2.98	2.50	2.58	2.15	2.20	22.11	8.47	15.05	6.7	3.89	7.78	6.29	6.01	7.87	10.57	10.85	12.17	7.63	2.75	15.21	7.98
Hy		2.71	2.34	2.24	2.82	2.95	2.87	2.90	38.99	16.55	30.17	15.31	13.75	20.58	17.02	14.90	21.47	14.47	18.13	20.09	21.76	2.775	28.57	17.77
Ilm		0.11	0.09	0.10	0.17	0.13	0.17	0.15	4.06	1.75	2.22	0.55	1.10	0.74	1.61	1.42	1.65	1.54	1.41	1.67	1.61	0.12	2.68	1.33
Ap		0.23	0.25	0.28	0.25	0.25	0.28	0.28	0.07	0.35	0.19	0.12	0.28	0.30	0.21	0.25	0.44	0.39	0.35	0.49	0.49	0.265	0.20	0.32

FeO* is total FeO; Kiel = Kiel University; Xeno = Xenolith; P-g = Per-aluminous granite; Grt = Garnet; Crd = Cordierite; MDL: Method Detection Limit.

Table 1: Representative whole rock geochemical analyses (XRF) of major elements of Chah-Bazargan rocks along with CIPW norm.

of powders weights was then calculated. Method Detection Limits (MDL) are determined by the X-ray florescence lab. For trace elements, fourteen samples were analysed with an AGILENT 7500cs ICP–MS (inductively coupled plasma-mass spectrometry) instrument at the University of Kiel, Germany, and six samples were analysed with an ICP–MS instrument at the ALS Chemex Company of Canada (Table 2). Method Detection Limits (MDL) were determined by the ICP–MS lab.

Mineral chemistry

Garnet

Garnet from all the meta-pelitic xenoliths has a narrow range in Mg, Fe, Ca and Mn contents, and is characterized by Fe-rich compositions and flat zoning profiles. Garnet from Grt–Crd–Sil meta-pelitic xenoliths displays higher Mg content with wide cores that have uniform compositions (approximately Alm_{79}, Prp_{13}, Sps_{06}, Grs_{04}) and rims up to 0.5 mm wide, displaying a smooth increase in Mn and decrease in Mg with constant Fe and Ca (Fig. S1a). Garnet from Grt–Crd-bearing meta-pelitic xenoliths is slightly zoned and contains higher Mn (Alm_{67}, Prp_{08}, Sps_{22}, Grs_{04}) (Fig. S1b). It also shows a slight increase of Fe and Mn towards rims indicating retrogression. Garnet of peraluminous granites is weakly zoned and shows a slight increase in Fe from the core to the inner rim and then a slight decrease from the inner rim towards the outer rim as well as a slight decrease in Mn from the core to the inner rim and then a slight increase from the inner rim towards the outer rim with constant Mg and Fe, suggesting retrogression (Fig. S1c).

Cordierite

The Mg# (=100× atomic $Mg/(Mg+Fe^{+2})$) values of cordierite in several meta-pelitic xenoliths are in the range of 49 to 56. In some xenoliths, Mg content of cordierite decreases from the core to the rim. Some meta-pelitic xenoliths have ~75 % cordierite, suggesting that they are residues after partial melting or reflect an unusual starting bulk composition. Cordierite composition in peraluminous granite is broadly similar to that in the meta-pelitic xenoliths.

Sample		140-1	187	190-B	189-E	260	264	272	181-E	182-E2	183-E1	188-E1	189-E3	190-E1	191-E5	192-E2	193-E3	111-c	114-a	220	221	Average of Granite	Average of migmatite Xenolith	Average of metapelite & Xenolith	Average of Shale Li, 2000
Rock type		P-g	P-g	P-g	P-g	P-g	P-g	P-g	Xeno	Xeno	Xeno	Xeno	Xeno	Xeno	Xeno	Xeno	Xeno	Pelite	Pelite	Pelite	Pelite				
	MDL	Grt	Grt	Grt	Grt	Crd	Crd	Crd	Mig	Mig	Mig														
	wt.%	Kiel	Kiel	Kiel	Kiel	Kiel	Kiel	Kiel	Kiel	Kiel	Kiel	Kiel	Kiel	Kiel	CCC	CCC	Kiel	CCC	CCC	CCC	CCC				
V	0.2	3.32	2.23	2.85	5.05	6.65	7.59	7.32	266.33	138.90	185.42	64.41	85.25	112.20	106.2	73.6	98.32	108.2	137.7	123.1	110.7	5.00	196.88	101.97	130.00
Cr	0.1	1.06	0.89	0.97	2.46	2.89	3.23	2.12	153.54	79.94	94.01	64.61	58.60	74.13	60.2	81.1	71.43	69.4	58.6	82.7	75.3	1.95	109.16	69.61	90.00
Co	0.1	0.69	0.49	0.88	1.02	0.95	0.77	0.59	30.24	14.06	19.73	8.97	10.12	17.98	12.1	14.2	15.59	18.2	13.1	10.3	14.1	0.77	21.34	13.47	19.00
Ni	0.1	0.91	1.08	1.12	1.62	1.55	1.30	1.41	106.11	34.16	62.31	25.48	19.87	32.54	30.5	34.4	31.58	31.2	46.4	22.9	38.8	1.28	67.53	31.37	50.00
Rb	0.1	165.12	144.19	148.56	114.38	138.95	157.08	165.05	67.66	132.61	88.47	47.81	40.32	54.17	77.1	39.5	54.67	114.1	75.3	85.6	63.5	147.62	96.25	65.21	140.00
Sr	0.5	6.08	6.28	5.69	15.04	11.21	7.54	13.17	43.25	102.21	80.25	52.49	75.71	41.21	69.4	68.9	58.62	47.4	79.5	94.1	83.7	9.29	75.24	67.10	170.00
Y	0.1	3.78	3.54	4.56	6.31	7.42	5.57	6.14	53.41	26.60	35.34	43.55	51.13	67.14	55.8	55.2	59.12	38.3	53.7	48.9	65.4	5.33	38.45	53.82	26.00
Zr	0.1	65.12	55.29	49.67	46.60	55.15	50.81	44.42	352.27	175.40	241.31	178.87	191.32	219.31	263.3	155.7	207.32	148.6	174.3	170.5	193.8	52.44	256.33	190.30	160.00
Nb	0.1	42.85	32.22	38.65	4.22	4.58	3.43	3.93	38.41	13.77	19.12	9.14	12.15	31.24	21.3	17.6	20.12	25.3	51.6	43.7	34.8	18.55	23.77	26.70	11.00
Ba	1.0	36.78	47.43	43.15	76.43	58.99	24.25	66.08	132.92	389.15	120.31	54.24	72.61	157.19	187.3	122.3	131.54	432.1	201.5	345.6	398.3	50.44	214.13	210.27	580.00
La	0.1	0.87	0.96	1.08	1.40	1.27	1.14	1.32	47.33	34.34	40.27	15.76	13.20	32.74	28.4	18.7	25.24	39.2	31.3	44.8	50.9	1.15	40.65	30.02	43.00
Ce	0.1	4.39	4.12	5.12	6.03	5.87	5.55	5.06	98.18	66.96	76.48	31.26	30.15	65.34	58.2	42.1	52.12	64.1	60.3	79.7	83.2	5.16	80.54	56.65	82.00
Pr	0.02	0.31	0.26	0.23	0.45	0.40	0.36	0.41	11.32	8.37	10.26	3.88	4.45	8.43	7.5	6.1	7.21	6.8	8.3	9.8	11.2	0.35	9.98	7.37	9.80
Nd	0.3	0.88	0.97	1.13	1.77	1.46	1.37	1.58	41.77	31.40	35.89	14.52	17.89	32.12	29.4	21.4	25.71	27.3	34.1	32.5	41.8	1.31	36.35	27.67	33.00
Sm	0.05	0.35	0.28	0.30	0.63	0.50	0.46	0.54	7.37	6.11	6.73	3.26	5.07	8.49	7.1	4.9	7.33	5.2	8.3	7.4	9.1	0.44	6.74	6.62	6.20
Eu	0.02	0.05	0.03	0.04	0.07	0.05	0.04	0.06	0.37	1.20	0.71	0.66	1.02	1.31	1.2	0.8	1.21	0.94	1.3	1.1	1.5	0.05	0.76	1.10	1.20
Gd	0.05	0.41	0.34	0.49	0.79	0.62	0.57	0.67	7.33	5.50	6.63	4.19	6.27	9.28	8.9	6.4	8.07	6.3	8.5	7.6	9.8	0.56	6.49	7.53	5.10
Tb	0.01	0.07	0.08	0.09	0.18	0.17	0.13	0.15	1.44	0.84	1.12	0.91	1.25	2.02	1.8	1.2	1.67	1.2	1.8	1.6	2.1	0.12	1.13	1.56	0.84
Dy	0.05	0.71	0.62	0.67	1.18	1.07	0.96	1.11	10.30	5.08	7.24	6.87	8.45	12.83	11.3	9.1	11.09	7.6	11.5	9.8	13.5	0.90	7.54	10.20	4.70
Ho	0.02	0.14	0.13	0.15	0.23	0.20	0.19	0.22	2.20	1.03	1.57	1.54	1.88	2.75	2.5	1.9	2.37	1.7	2.5	2.2	2.9	0.18	1.60	2.22	1.10
Er	0.03	0.51	0.43	0.40	0.65	0.63	0.56	0.61	6.29	2.86	3.93	4.46	5.68	7.56	6.7	5.8	6.73	5.2	7.5	6.4	8.2	0.54	4.36	6.42	3.00
Tm	0.01	0.07	0.08	0.09	0.11	0.11	0.09	0.10	0.96	0.43	0.59	0.68	0.87	1.15	1.0	0.9	0.92	0.8	1.2	0.9	1.2	0.09	0.66	0.96	0.44
Yb	0.05	0.64	0.69	0.76	0.84	0.76	0.65	0.69	6.35	2.91	3.79	4.44	5.79	7.71	6.7	5.5	6.46	5.1	7.5	6.2	8.4	0.72	4.35	6.38	2.80
Lu	0.01	0.12	0.10	0.14	0.12	0.11	0.09	0.09	0.94	0.43	0.60	0.66	0.87	1.13	1.0	0.8	0.91	0.8	1.1	0.9	1.2	0.11	0.66	0.94	0.42
Hf	0.1	3.12	2.37	2.75	2.23	2.50	2.21	1.88	10.95	5.33	4.89	5.72	4.84	9.78	7.6	6.3	8.41	6.3	8.6	8.1	9.8	2.44	7.06	7.55	5.00
Ta	0.1	2.68	2.16	3.11	1.120	0.89	0.40	0.72	3.11	0.98	2.46	0.94	1.37	2.68	1.8	1.5	2.25	2.7	2.5	2.9	3.4	1.58	2.18	2.20	1.30
Pb	0.1	15.25	17.46	20.12	25.92	20.45	14.47	13.39	5.26	24.59	18.34	13.51	19.87	21.23	29.7	16.4	23.55	17.7	20.8	24.2	28.7	18.15	16.06	21.57	20.00
Th	0.2	1.14	0.90	1.39	2.67	2.24	1.91	1.76	18.93	13.92	15.72	9.73	10.68	14.28	11.5	9.1	15.88	13.1	14.2	16.4	12.2	1.72	16.19	12.71	12.00
U	0.1	0.72	0.90	1.01	2.24	1.52	0.88	0.68	1.68	2.11	2.04	2.11	2.61	2.75	2.3	2.5	2.71	2.3	3	1.8	2.1	1.14	1.94	2.42	2.70
Ti		751	626	626	1126	876	1126	1001	26783	11514	14643	3630	7259	4881	10638	9387	10889	10138	9262	11014	10638	876	17647	8773	4600
P		704	775	845	775	775	845	845	211	1057	564	352	845	916	634	775	1339	1198	1057	1479	1479	795	611	1007	700
K		63166	65820	64759	53612	55310	53505	54142	18684	41403	16455	18047	27071	43739	41085	31212	44376	72296	24736	39811	43420	58616	25514	38579	28239
Na		44367	39582	50457	64158	59374	62418	61548	17181	38930	18269	46977	62636	53067	37625	39365	42192	9352	34363	37190	41975	54558	24793	40474	12832
Rb/St		27.16	22.96	26.11	7.61	12.40	20.83	12.53	1.56	1.30	1.10	0.91	0.53	1.31	1.11	0.57	0.93	2.41	0.95	0.91	0.76	18.51	1.32	1.04	0.82
Rb/Ba		4.49	3.04	3.44	1.50	2.36	6.48	2.50	0.51	0.34	0.74	0.88	0.56	0.34	0.41	0.32	0.42	0.26	0.37	0.25	0.16	3.40	0.53	0.40	0.24
K/Ba		1717.4	1387.7	1500.8	701.4	937.6	2206.4	819.3	140.6	106.4	136.8	332.7	372.8	278.3	219.4	255.2	337.4	167.3	122.8	115.2	109.0	1324.4	127.9	231.0	48.69
Eu*		0.11	0.09	0.12	0.21	0.17	0.15	0.18	2.16	1.71	1.97	1.10	1.67	2.62	2.36	1.67	2.27	1.70	2.47	2.21	2.78	0.15	1.95	2.09	1.66
Eu/Eu*		0.30	0.22	0.23	0.22	0.20	0.18	0.22	0.11	0.47	0.24	0.40	0.41	0.33	0.34	0.32	0.36	0.37	0.35	0.33	0.36	0.22	0.26	0.35	0.48
La_n/Yb_n		0.14	0.18	0.14	0.22	0.22	0.24	0.28	0.94	1.50	1.26	0.45	0.28	0.54	0.53	0.44	0.52	0.92	0.53	0.93	0.80	0.20	1.16	0.60	1.92
La_n/Sm_n		0.54	0.75	0.79	0.49	0.56	0.54	0.53	1.40	1.23	1.31	1.06	0.57	0.84	0.88	0.83	0.75	1.65	0.82	1.32	1.22	0.57	1.32	0.99	1.52
Gd_n/Yb_n		0.43	0.33	0.43	0.63	0.54	0.58	0.65	0.77	1.26	1.17	0.63	0.72	0.80	0.89	0.78	0.83	0.82	0.76	0.82	0.78	0.52	0.99	0.79	1.21
Sm_n/Yb_n		1.33	1.28	1.17	2.20	1.97	0.34	0.26	0.25	0.47	0.41	0.44	0.49	0.73	1.32	1.12	0.46	0.55	0.69	0.67	0.56	0.75	0.70	0.64	0.71

Kiel = Kiel University; CCC=ALS Chemex Company of Canada; Xeno = Xenolith; P-g = Per-aluminous granite; Mig = Migmatite; Grt = Garnet; Crd = Cordierite; MDL: Method Detection Limit.

Table 2: Representative whole rock geochemical analyses (ICP-MS) of minor and rare earth elements of the Chah-Bazargan rocks.

Biotite and muscovite

Biotite from different rock types has a wide range of compositions (Fig. S2; Table S3). It is more enriched in Mg in meta-pelitic xenoliths compared to the peraluminous granites, suggesting that biotite in peraluminous granite may have crystallized from magma or changed in composition due to restite-melt back reaction (also see Erdmann et al. 2009; Taylor & Stevens 2010 for more information). In addition, the biotite might also change composition because it has reacted with the very large volume of granite around it (Lavaure & Sawyer 2011). Biotite in meta-pelitic xenoliths and contaminated quartz diorite is similar in composition, suggesting that biotite in the contaminated quartz diorites is not a result of magmatic crystallization and so must have come from the meta-pelitic xenoliths in the host magma. Biotite from meta-pelitic xenoliths with many veins (diatexite) has much higher Ti content than meta-pelitic xenoliths lacking such veins (without migmatitic structure). This is probably due to higher metamorphic temperature (see Henry & Guidotti 2002 for more discussion) of the diatexite. Biotite in all rock types have a wide range of Ti, which might be due to diffusional exchange, so that it is confirmed by very small grains of ilmenite within biotite coronas around garnet which are a result of retrograde reactions after magma solidification.

Muscovite in all rock types, both prograde and retrograde, has a similar composition (Table S3).

Spinel, ilmenite, and apatite

All analysed spinel grains are rich in $FeAl_2O_4$ component, with Cr (~0.07 p.f.u.) and relatively high Zn (~0.55 p.f.u.). Hercynite (spinel) from matrix is similar to that included in cordierite.

All analysed ilmenites have compositions close to the $FeTiO_3$ end-member (Table S3). Apatite from all rock types has higher Mn and F but lower Cl contents.

K-feldspar

Many K-feldspar grains are perthitic. Perthitic K-feldspar has a re-integrated composition of X_{kfs} 0.85–0.88. These compositions were calculated by analyses of BSE images and point-counting of the perthite.

Plagioclase

Plagioclase has a wide range of Ca and Na contents (Fig. S3). In quartz-diorites, plagioclase is andesine and shows a narrow range of Ca and Na and a slight decrease in Ca and increase in Na near the rim, but the main part of their profiles are approximately flat (Table S3; Fig. S3a). Plagioclase grains from contaminated quartz diorites are also mostly andesine, showing a flat profile and a main decrease in Ca content near the rim. Other plagioclase grains (Fig. S3a–c) have different profiles, and indicate a pronounced decrease in Ca from the core towards the rim, then a sharp increase in Ca towards the outermost part of the rim, suggesting a magma mixing process (Fig. S3b). In cordierite-rich metapelitic xenoliths (nebulitic migmatites; diatexite), plagioclase is mostly andesine but shows a decrease in Ca near the rim (Fig. S3c). Plagioclase in the peraluminous granites (Fig. S3d) indicates a profile similar to that from contaminated quartz diorites, but more enriched in Na (oligoclase). The cores from the peraluminous granite shown in Fig. S3d are substantially less calcic compared to the plagioclase from the quartz diorite. The plagioclase core of rocks may have been a part of plagioclase minerals crystallized from primary quartz dioritic magma. It is possible that the amount of calcium in cores of plagioclase from the peraluminous granite has fallen due to diffusion (see also García-Arias & Stevens (2017a,b) and Moyen et al. 2017 for more discussion).

Oscillatory zoning occurs within both core and rim domains (e.g., Fig. 3c, e). Such zoning patterns are normally present only in plagioclase of igneous rocks, rim wards enrichment in Na is commonly interpreted as reflection of decreasing temperatures during fractional crystallization. Therefore, these zoning patterns strongly suggest that plagioclase in all rock types, especially in metapelitic xenoliths, crystallized in the presence of melt, with rims crystallized during cooling, and also indicate that plagioclase with oscillatory zoning surrounded the cordierite and biotite (Fig. 3c,e). These observations indicate that melt was present in the metapelitic xenoliths.

Geothermobarometry

In this section thermobarometry has been used to estimate the peak *P–T* conditions of metamorphism in the studied metapelitic xenoliths and peraluminous granites. These results provide information about (1) the conditions of partial melting in metapelitic xenoliths, and (2) the crustal level of emplacement of the quartz diorite.

Kriegsman (2001) discussed that the ultimate effect of migmatization comes from four successive processes: prograde partial melting; melt extraction close to peak temperatures; incomplete retrograde reactions between restite and in situ crystallizing melts; and crystallization of remaining melt at the solidus. Mineral assemblages formed in the peak and retrograde metamorphic stages of the Chah-Bazargan migmatitic xenoliths are Bt+Grt+Sil+Crd+Spl+Crn+Pl+Kfs+Qtz (Fig. 2a–g,i,j) and Ms+Chl+fibrous Sil+Qtz, respectively. Based on Kriegsman (2001) and White and Powell (2002), retrograde mineral assemblage in anatectic migmatites is a result of partial retrograde reactions (back reaction) between in situ crystallizing melt and restite. Kriegsman & Hensen (1998) demonstrated that back reaction has significant implications for geothermobarometry. For this reason, suitable minerals, near the peak temperatures for geothermobarometry, were selected. The minerals were chosen from sections far from retrograde mineral assemblages. Analytical point of the

different minerals such as garnet, plagioclase, and biotite were defined on the basis of parts close to the peak temperatures and chemical compositions (Table S3) and profiles of different minerals (Figs. S1–S3). To investigate the peak metamorphic conditions, garnet with high pyrope component, biotite with low X_{Fe} and high Ti level and plagioclase with high anorthite component were selected.

Peak metamorphic conditions of regional metamorphic rocks to the southwest of the Chah-Bazargan quartz diorite, in the Qori metamorphic complex, were estimated by Fazlnia et al. (2007) using several conventional geothermobarometers, such as Grt–Ky–Qtz–Pl (GASP), Grt–Bt–Pl–Qtz, Grt–Ms–Pl–Qtz, Grt–Pl–Bt–Ms and Grt–Hbl–Pl–Qtz barometers and Grt–Bt, Grt–Hbl and Hbl–Pl thermometers. The peak pressure and temperature of regional metamorphism in the Seghalaton outcrop of QMC (eastern part of the study area; Fig. 1) at 187 to 180 Ma were estimated to be 7.5±1.2 kbar and 660±40 °C (Fazlnia et al. 2007, 2009). The pressure estimation allows depth of burial to be estimated at ca. 29 km. Following the emplacement of the intrusion, a secondary metamorphic event affected the QMC at 147 Ma due to the initiation of Neotethyan mid ocean ridge subduction beneath the southern Sanandaj–Sirjan zone. Trondhjemitic dykes were created as a result of this event (Fig. 1). The peak *P–T* estimations of the arc-related metamorphism are 9±1.2 kbar and 700±30 °C (Fazlnia et al. 2009; also see Sheikholeslami 2015).

Peak metamorphic contact conditions in metapelitic xenoliths and peraluminous granites were estimated using conventional calibrated thermobarometers, thermometric diagrams are shown in (Fig. 4). The calibrations include the Grt–Bt thermometers (Thompson 1976; Holdway & Lee 1977; Ferry & Spear 1978; Hodges & Spear 1982; Perchuk & Lavrent'eva 1983; Dasgupta et al. 1991; Bhattacharya et al. 1992; Gessmann et al. 1997; Kaneko & Miyano 2004; Table S4), and Grt–Sil–Pl–Qtz (Hodges & Spear 1982) and Grt–Bt–Pl–Qtz (Wu et al. 2004), barometers (Table S5). A thermometric diagram of Zr-M index (Watson & Harrison 1983) was used for peraluminous granites (Fig. S4). On the basis of X_{Fe} in cordierite (Thompson 1976), metapelitic xenoliths and peraluminous granites, which include assemblage Grt–Crd–Sil–Qtz (Table S2), are plotted at pressures between 4.5 and 5.5 kbar (Fig. 4).

The current thermobarometeric results are based on mineral core compositions of matrix phases. The thermobarometric results estimate peak *P–T* conditions for metapelitic xenoliths, peraluminous granite and partial melting of metapelitic xenoliths to be ~4.5±1.0 kbar and ~760±35 ºC (Fig. 4). The temperature value is in agreement with petrographic evidence for the initiation of hydrate breakdown melting of biotite in the presence of garnet and sillimanite (Fig. 3a–b) and overlaps with the field of biotite melting dehydration (Fig. 4).

Rock geochemistry

Peraluminous granites have restricted SiO_2 contents between 73–75 wt. %. CaO and MgO between 0.56–0.72 wt. %. and 0.11–0.31 wt. %, respectively. K_2O+Na_2O have a range between 6.5 and 8 wt. %. These granites are enriched in Rb, Zr, Ba and Pb and depleted in Ni, Cr, V, Nd, Sr, Y, Nb, and have REE contents comparable to S-type granites (Brown 1994; Harris et al. 1995; Bea 1996b; Patiño Douce 1999; Nabelek & Bartlett 2000; Healy et al. 2004; Stevens et al. 2007; Villaros et al. 2009; García-Arias et al. 2012; Moyen et al. 2017). Low concentrations of Ni, Cr, V, Sr, Y, Nb, and REE indicate that they probably remained in the residuum (metapelitic xenoliths) during partial melting and segregation. Based on Brown (1994), Brown (2007), García-Arias et al. (2012), Brown (2013), Sawyer (2014), and García-Arias & Stevens

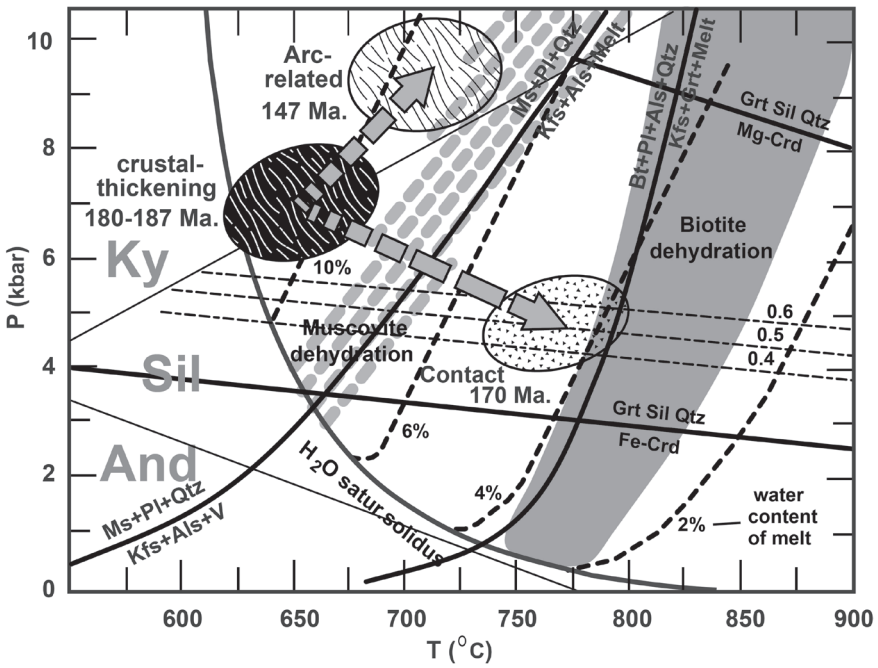

Fig. 4. Thermobarometric constraint on the *P–T* evolution of the Chah-Bazargan migmatitic xenoliths and peraluminous granites. Thin horizontal dashed lines of X_{Fe} cordierite values are after Thompson (1976). Wet granite solidus, approximate ranges of dehydration of micas in presence of quartz and plagioclase and minimum contents of felsic melts; modified from Patiño Douce & Harris (1998), Holtz & Johannes (1994) and Spear (1993). Three ellipsoid fields represent crustal-thickening regional metamorphism which occurred 187–180 Ma, contact metamorphism 173 Ma, which is related to intrusion of the Chah-Bazargan batholith, and arc-related regional metamorphism that occurred 147 Ma.

(2017a, b) several potential factors that may control the composition of the S-type magmas include: melt loss, batch and fractional melting, spatially restricted equilibration of plagioclase during partial melting and the nature and amount of the entrained mineral assemblage.

The presence of normative corundum (Table 1) indicates that these granites are peraluminous, as seen in Fig. 5. All granites plot in the range of peraluminous granites (Fig. 5) and were probably extracted from migmatitic felsic metapelite-metagraywacke (Fig. 6). Leucocratic peraluminous granites are divided into garnet-bearing and cordierite-bearing granites based on main minerals of the rocks.

In REE and multi-element plots, garnet-bearing and cordierite-bearing granites have approximately the same patterns (Figs. 7a, 8a, S5). The garnet-bearing granites are slightly enriched in REE in comparison with cordierite-bearing ones (Fig. 8; Table 2). Also, there are higher U but lower Nb and Ta values in the cordierite granites relative to the garnet granites (Figs. 7a, 8a), additionally, the garnet granites have, unexpectedly, rather lower HREE contents (Fig. 7a; Table 2).

The Chah-Bazargan peraluminous granites are characterized by lower LREE but higher HREE contents and consequently lower La_n/Yb_n, La_n/Sm_n and Gd_n/Yb (Table 2) in comparison with common peraluminous granites (see Brown, 1994 for more discussions). Garnet-bearing granites show negative-Eu anomaly (Eu/Eu*=0.25) and are slightly enriched in HREE in comparison with cordierite-bearing granites, especially Yb and Lu, reflecting the presence of garnet. All peraluminous granites have negative-Eu anomaly similar to metapelitic xenoliths but less pronounced. Negative-Eu anomalies in granites and also negative-Eu and -Sr anomalies in migmatitic xenoliths, schist xenoliths, and metapelites show that plagioclase was not involved in partial melting reactions of metapelitic xenoliths or had low percentages of contributions and/or it resulted from protolith composition, and also that negative-Eu and -Sr anomalies in granites resulted from the protolith. Peraluminous granites show negative-La anomaly because of few monazite grains in many metapelitic rock types from the study area. The REE plots show that these rocks have a Ce peak rather than La anomaly, reflecting the enrichment of the source (Figs. 8a, 9a, S5).

Negative-Ba anomalies in all rock types (Figs. 7, S5) show that abundance of Ba resulted from the protolith (metapelitic xenoliths). Positive-K anomaly in granites, metapelitic xenoliths, and metapelites is due to K-bearing phases such as K-feldspar and muscovite, which are still stable in all rocks.

Averages of Qori metamorphic metapelite and schist xenoliths plots between migmatitic xenoliths and peraluminous granites can be seen in Fig. 5. Therefore, decrease in K and Na and increase in Fe and Mg in the migmatitic xenoliths are consistent with partial melting and melt extraction from pelitic xenoliths with the mafic minerals such as garnet and cordierite remaining in the residue.

Total REE, Y, Zr, Hf, Sr, Ba, Th, U, Ti and Nb in the Chah-Bazargan peraluminous granites is lower than in the metapelites, metapelitic xenoliths and migmatitic metapelitic

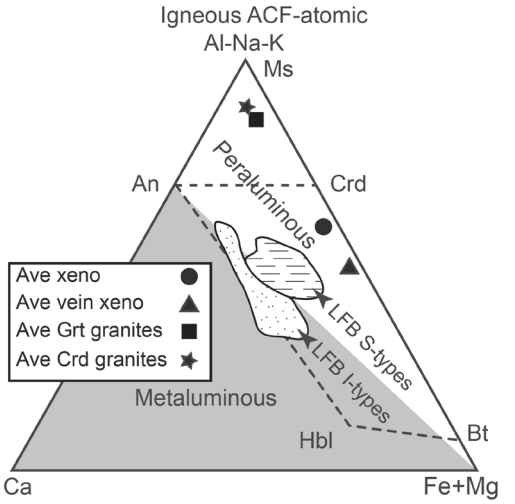

Fig. 5. ACF (*A* is Al_2O_3–(Na_2O+K_2O), *C* is CaO, and *F* is FeO^{total}+MgO) plot delineating fields (Healy et al. 2004) for the Chah-Bazargan granites, migmatitic xenoliths, and metapelites and xenoliths without migmatite texture.

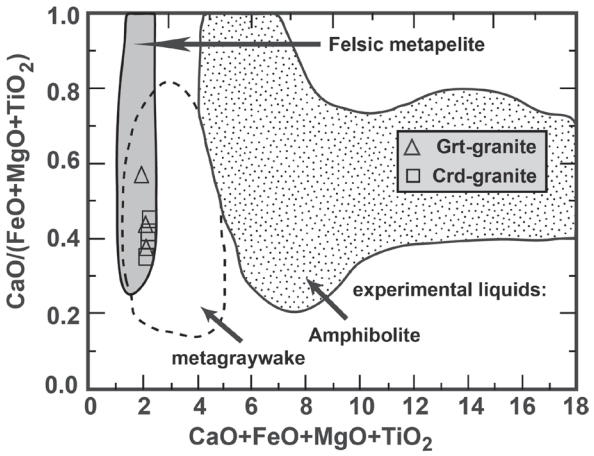

Fig. 6. Compositions of the study granites compared to melts produced by experimental dehydration melting of metasedimentary rocks (fields of melt compositions after Patiño Douce 1999).

xenoliths (Fig. S5). Melts extracted from the metapelitic migmatites are depleted in trace elements such as Rb, Zr, Th, U, Y, and REE, in order to be equivalent to granite plutons and batholiths in the upper crust (Bea 1996a; Sawyer 1996; Sheppard et al. 2003). Stability of minerals such as garnet, cordierite, ilmenite, zircon, and monazite in the residuum during partial melting causes them to be depleted during melt extraction.

Discussion

Modelling

Decrease of SiO_2, P_2O_5, Na_2O, and K_2O and increase of Al_2O_3, TiO_2, MgO, and FeO* in migmatitic xenoliths in comparison with metapelitic xenoliths and metapelites

demonstrate that residual minerals were stable phases of migmatitic xenoliths during partial melting. In contrast, other minerals were unstable phases during partial melting reactions and formed felsic parts of migmatites and small patches of peraluminous granites.

Geochemical melting models based on both batch and Rayleigh melting modelling can be used to determine the possible amount of partial melting in the migmatitic xenoliths. Sawyer (1991), Acosta-Vigil et al. (2006), Brown (2007), Yakymchuk & Brown (2014), and García-Arias & Stevens (2017a) have discussed the most important factors influencing the composition of the peraluminous melts such as equilibrium and fractional melting and crystallization during partial melting and crystallization, flow segregation, gravitational settling, filter-pressing fractionation, the amount of water in the original magma, path of emplacement and cooling, mineral assemblage of the protolith, and *P–T* conditions. Based on presence and movement of melt in contact with the initial protolith (Figs. 2, 3a–b) batch melting equations (Shaw 1970) can be used for the Chah-Bazargan migmatitic xenoliths. Melting was modelled using the equilibrium batch melting equation:

$$\frac{C_i^{\ell}}{C_i^0} = \frac{1}{D(1-F)+F}$$

$$\frac{C_i^{s}}{C_i^0} = \frac{D}{F+D(1-F)}$$

where i is the element of interest, C_i^0 is the original concentration in solid phase (and the concentration in the whole system), C_i^{ℓ} is the concentration in the liquid (or melt), C_i^{s} is the concentration remaining in the solid, F is the melt fraction (i.e. mass of melt/mass of system) and D is partition coefficient of the interested element: $D = C_i^{s}/C_i^{\ell}$.

These equations are extremely useful in describing the relative enrichment or depletion of a trace element in the liquid as a function of melting degree.

The averages of metapelites, peraluminous granites, and migmatitic xenoliths trace elements were used. Thus, the concentrations of various elements of

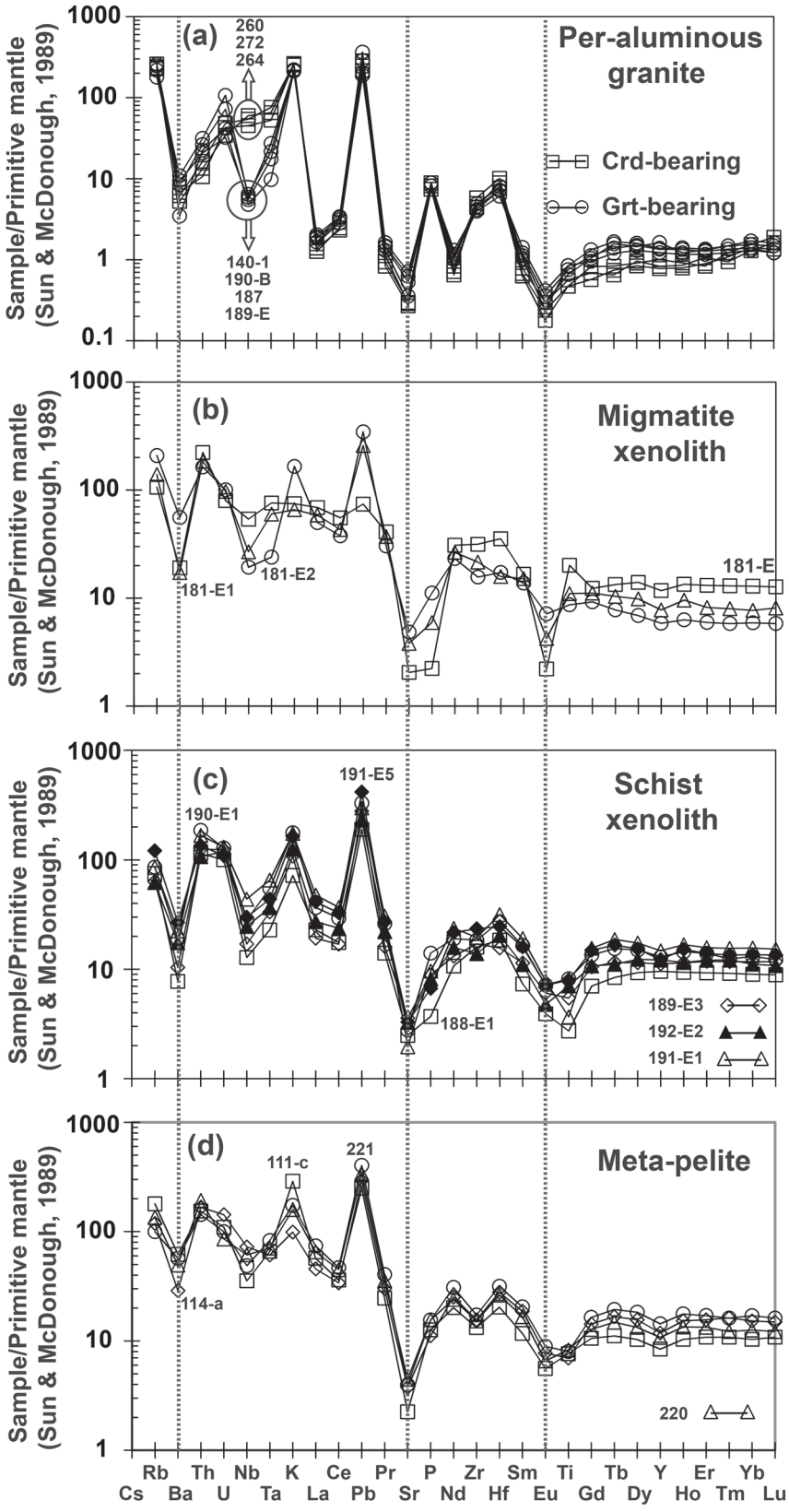

Fig. 7. Continental crust normalized multi-element plots of Chah-Bazargan batholith samples. **a** — Normalized multi-element diagram of peraluminous granites; **b** — Normalized multi-element diagram of metapelitic migmatitic xenoliths; **c** — Normalized multi-element diagram of schist xenoliths; **d** — Normalized multi-element diagram of metapelites from the Qori metamorphic complex. Normalization values after Taylor & McLennan (1985).

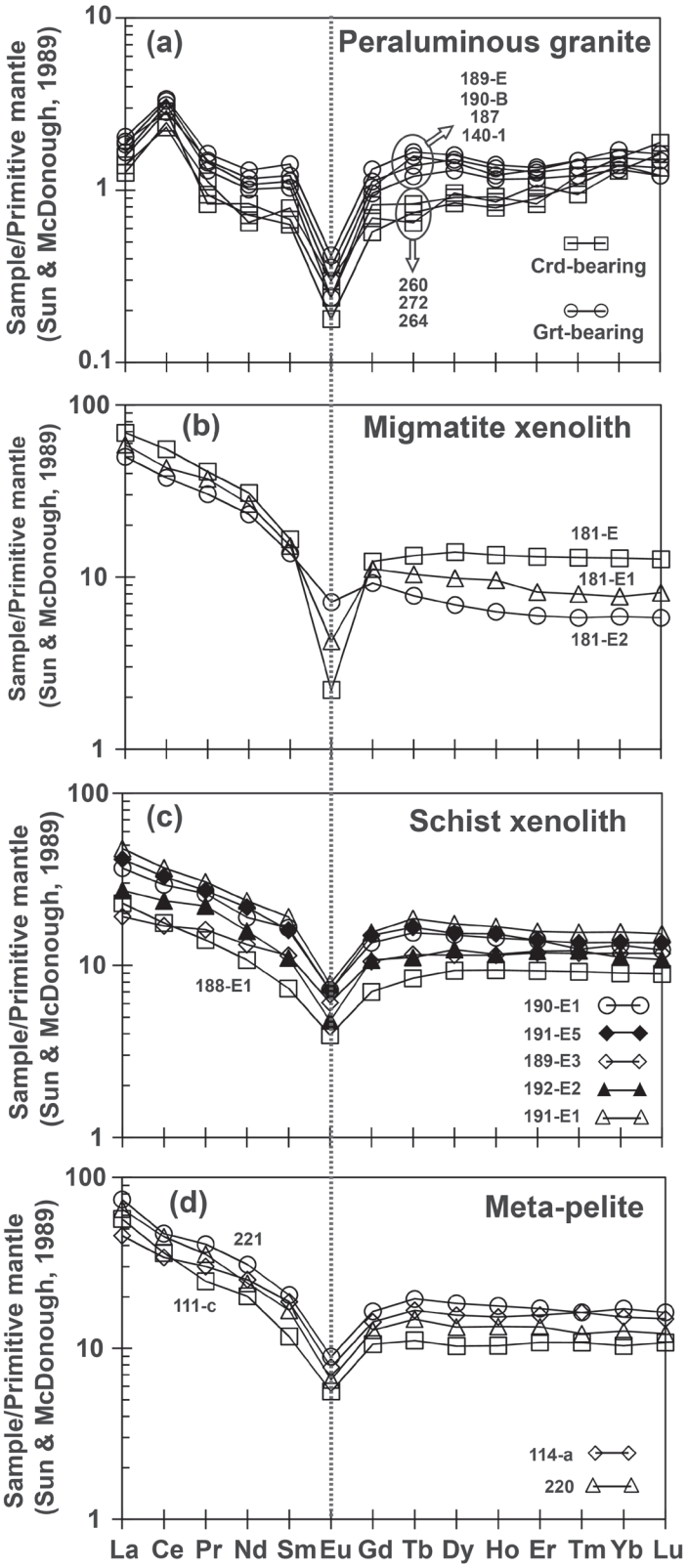

Fig. 8. Continental crust normalized REE plots of Chah-Bazargan batholith samples. **a** — Normalized REE diagram of peraluminous granites; **b** — Normalized REE diagram of metapelitic migmatitic xenoliths; **c** — Normalized REE diagram of schist xenoliths; **d** – Normalized REE diagram of metapelites from the Qori metamorphic complex. Normalization values after Taylor & McLennan (1985).

average initial protolith (C_i^0; metapelitic xenoliths and metapelites), peraluminous granite (C_i^t), and relict protolith (C_i^s; as restite=migmatitic xenoliths) were considered (Tables 1, 2). The average composition of shale (Li 2000) was used for modelling because the Chah-Bazargan peraluminous granites are plotted in the field of metagraywackes-felsic metapelites (Fig. 6).

Partial melting

According to Fig. S5, the patterns of metapelitic xenoliths and metapelites were compared to shale. The Chah-Bazargan peraluminous granites were used as melt compositions (Tables 1, 2). Levels of the migmatitic xenolith elements have not been altered (Table S6; for more details see Champion & Smithies 2007).

Simple trace-element modelling was used to test whether the Chah-Bazargan peraluminous granites bear compositions that are consistent with derivation by partial melting at low pressures (4.5 kbar; the upper amphibolite facies) from a migmatitic metapelitic (xenolith) source. Bulk partition coefficients were calculated assuming 1 %, 5 %, 10 %, 20 %, 30 %, 40 %, and 50 % partial melting (Table S7). Additionally, as a measure of suitability of the modelled source compositions, the degree of partial melting was calculated for highly incompatible elements and Cr assuming bulk partition coefficients calculated by partition coefficient of different elements for each mineral (see the following paragraphs; Table S8). Partition coefficients (K_d) of different elements are similar to those used above. For a full discussion of partition coefficients usage for modelling crustal melting see Harris et al. (2003).

We can infer from the results, summarized in Table S7, apparently the behaviour of all elements, such as the REEs (La to Lu). The HFSE (Ti, Zr, Ta, Nb, Th, U, Hf, Y), Ba, Pb, and Sr is largely insensitive to source enrichment, but sensitive to the amounts of main and accessory minerals in the residue (diatexitic migmatites). The abundance of garnet, biotite, plagioclase, apatite, ilmenite, zircon and monazite in the source has increased the values of bulk partition coefficients for all the elements considered above (C_i^s/C_i^0). Therefore, the large proportion of these minerals were stable phases during partial melting of the source. Hence, partition coefficients increase with increasing levels of partial melting in the source (Table S7). Similar to this study, many studies of melts extracted from the migmatites indicate that these melts are excessively depleted in trace elements such as REEs, Nb, Rb, Zr, Th, U, and Y, to be the equivalent of granite plutons and batholiths in the upper crust (Bea 1996a; Sawyer 1996; Sheppard et al. 2003).

The behaviour of Na, K, and Rb is quite sensitive to the proportions of main minerals such as biotite,

muscovite and K-feldspar in the residue (diatexitic migmatites). Abundance of these minerals in the source increases the bulk partition coefficients of the elements. Furthermore, decreases of these coefficients with increased degrees of melting would indicate that muscovite and less biotite would become unstable phases during partial melting of the source.

Considering more incompatible elements such as La, Ce, and Sm and compatible element Cr indicates that relatively moderate degrees (between 20 and 30 %) of partial melting are permissible (Table S8). Concentrations of LREEs such as La, Ce, and Nd and Cr in geochemical modelling of the migmatitic xenoliths (C_i^s) demonstrate that degrees of partial

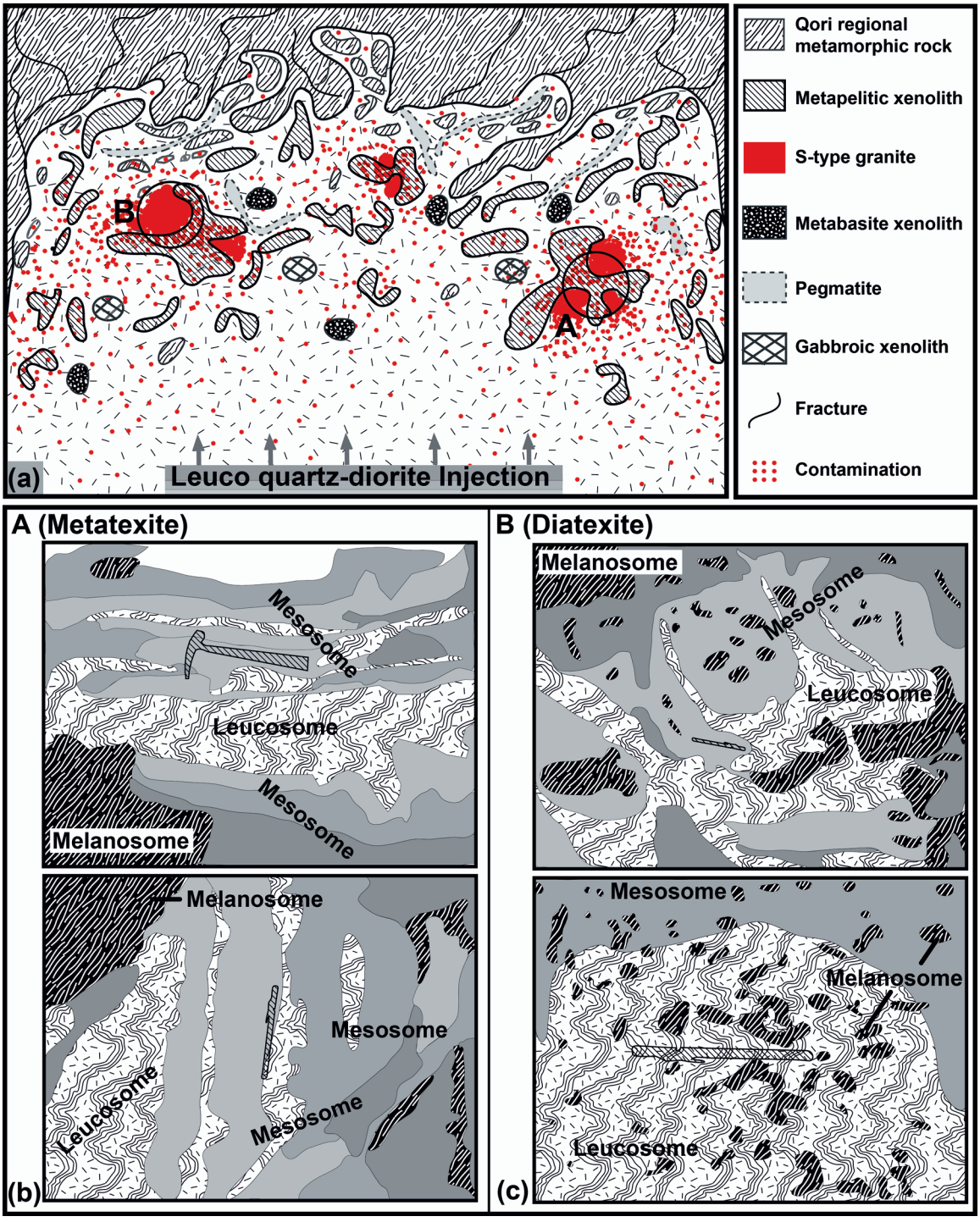

Fig. 9. Schematic model of the most important processes described in the Chah-Bazargan pluton. **a** — Schematic Figure which graphically summarizes the relationships between paleosome, melanosome, and neosome. **b** — Schematic relationships in the metatexites including representations of patch dilation, net, and stromatic structures. **c** — Schematic relationships in the diatexite including nebulitic, schollen, and schlieren structures. Figures (b) and (c) were plotted base on Figure 2.

melting between 20 and 30 % cause contents of these elements to be similar to the average of the observed concentrations of the elements (Table 2).

Partial melting of pelitic metasediments around the southwest contact of the Chah-Bazargan complex is a possible indication of advective heating as well as conductive transfer of heat by quartz diorite (Fig. 9). Balanced in situ crystallization, reactions between restite (mesosome) and melt (leucosome), and the adhesion force between melt (leucosome) and crystal (melanosome) prevent the melt separating from migmatitic xenoliths (Figs. 2, 3). Additionally, high viscosity of the magma and low temperature of the partial melting in the source were other important factors inhibiting melt extraction. It should be noted that mingling of some parts of peraluminious melt with quartz dioritic magma is possible (Fig. 9).

The volumes of peraluminous granite patches within the the Chah-Bazargan quartz-diorite intrusion are between several tens of centimetres to several tens of cubic metres. The patches are near or adjacent to the swarms of the migmatitic xenoliths. The aggregated migmatitic xenoliths are between several tens of centimetres to several metres across. Therefore, the maximum temperature of Chah-Bazargan intrusion has easily spread to the all parts of the xenoliths. Continuous injections of new quartz-dioritic magma to the chamber may also have served to maintain the high temperature. Convection and movement of the quartz-dioritic magma were important factors in aiding the separation and exhaustion of the leucosome components. As a result of processes, it is possible that only 20–30 vol. % of the melt could have left the migmatitic xenoliths and, so small patches of Chah-Bazargan peraluminous granites could be produced (Fig. 9a). Because the thermal and chemical composition of the melt was much different from the quartz-dioritic melt, the felsic melt remained as patches and did not mix into the quartz diorite.

Conclusion

Partial melting in the Chah-Bazargan metapelitic xenoliths, which are incorporated into the Chah-Bazargan quartz dioritic batholith (Fig. 9a) at 173 Ma, occurred at *P* and *T* conditions higher than the minimum melting curve of granite (ca. 4.5±1.0 kbar and 760±35 °C). A considerable volume of leucosome was generated, mostly as a stromatic type (Fig. 9b). Although these amounts of leucosomes do not represent pure melts, but contain entrained solid (residual, i.e. peritectic phases) material, textures and field relationships suggesting that the melt fraction was substantial. Melting reactions involved the incongruent breakdown of biotite. A portion of the leucosome (approximately 20–30 vol. %) was segregated from the diatexitic migmatitic xenoliths (Fig. 9c) during contact metamorphism and these amalgamated to produce small patches of the Chah-Bazargan peraluminous granites. A large part of the partial melts from migmatitic xenoliths could not be extracted due to a combination of situ crystallization, the adhesion force between melt and remaining crystal, and high viscosity of the magma.

Geochemical modelling indicates that in REEs plots, peraluminous melts are excessively depleted in trace elements such as REEs (La to Lu), HFSE (Ti, Zr, Ta, Nb, Th, U, Hf, Y), Ba, Pb, and Sr in comparison with xenoliths of migmatite. Furthermore, the modelling demonstrates that these elements are very sensitive to source enrichment and the amounts of major minerals such as garnet, biotite, muscovite, K-feldspar, plagioclase, and ilmenite, and accessory minerals, such as apatite, monazite, and zircon, in the residue of the diatexite migmatites. Hence, a portion of these elements were hosted by non-melted part of the mineral assemblage minerals considered before in the source (migmatitic xenoliths).

Acknowledgements: The authors would like to thank Prof. Dr. Volker Schenk, Dr. Peter Appel, Mrs. Barbara Mader, and Mrs. Astrid Weinkauf for their support during EMP and XRF analyses at Kiel University. Financial support from the Iranian Ministry of Science, Research and Technology, and Universities of Kerman and Urmia (Iran) and Institute für Geowissenschaften, Christian-Albechts-Universität zu Kiel (Germany) are gratefully acknowledged. Last but not the least, I would like to thank Prof. Robert J. Stern from the University of Texas at Dallas for English and scientific editing the article. This paper is dedicated to Afzalipour who founded Kerman University.

References

Acosta-Vigil A., London D. & Morgan G.B. 2006: Experiments on the kinetics of partial melting of a leucogranite at 200 MPa H_2O and 690–800 °C: compositional variability of melts during the onset of H_2O-saturated crustal anataxis. *Contrib. Mineral. Petrol.* 151, 539–557.

Agard P., Omrani J., Jolivet L. & Mouthereau F. 2005: Convergence history across Zagros (Iran): constraints from collisional and earlier deformation. *Geol. Rundsch.* 94, 401–419.

Agard P., Omrani J., Jolivet L., Whitechurch H., Vrielynck B., Spakman W., Monie P., Meyer B. & Wortel R. 2011: Zagros orogeny: a subduction-dominated process. *Geol. Mag*. 148, 692–725.

Akbari K., Tabatabaei Manesh S.M. & Safaei H. 2016: Tectonic Setting and Petrological Evidence for the Emplacement of Mylonitic Granites Within the Middle Part of Sanandaj–Sirjan Shear Zone from East and South East of Chadegan, Iran. *Geotectonics* 50, 313–326.

Alavi M. 1994: Tectonic of the Zagros orogenic belt of Iran: new data and interpretations. *Tectonophysics* 229, 211–238.

Ashworth J.R. 1985: Introduction. In: Ashworth J.R. (Eds.): Migmatites. *Blackie and Son*, 36–85.

Babaiea H.A., Ghazi A.M., Babaei A., La Tour T.E. & Hassanipak A.A. 2001: Geochemistry of arc volcanic rocks of the Zagros Crush Zone, Neyriz, Iran. *J. Asian Earth Sci*. 19, 61–76.

Bea F. 1996a: Controls on the trace element composition of crustal melts: Transactions of the Royal Society of Edinburg. *Earth Sci.* 87, 133–141.

Bea F. 1996b: Residence of REE, Y, Th and U in granites and crustal protoliths: implications for the chemistry of crustal melts. *J. Petrol.* 37, 521–552.

Bea F., Pereira M.D. & Stroh A. 1994: Mineral/leucosome trace-element partitioning in a peraluminous migmatite (a laser ablation — ICP-MS study). *Chem. Geol.* 117, 291–312.

Berberian F. & Berberian M. 1981: Tectono-Plutonic episodes in Iran. *Geol. Surv. Mineral. Explor. Iran*, *Report* 52, 566–593.

Berberian M. & King G.C.P. 1981: Towards a paleogeography and tectonic evolution of Iran. *Can. J. Earth Sci.* 18, 210–265.

Bhattacharya A., Mohanty L., Maji A., Sen S.K. & Raith M. 1992: Non-ideal mixing in the phogopiteannite binary: constraints from experimental data on Mg−Fe partitioning and a reformulation of the biotitegarnet geothermometer: *Contrib. Mineral. Petrol*. 111, 87–93.

Brown M. 1979: The petrogenesis of the St. Malo migmatite belt, Armorican Massif, France, with particular reference to the diatexites. *Neues Jahrb. Mineral. Abh.* 135, 48–74.

Brown M. 1994: The generation, segregation, ascent and emplacement of granite magma: the migmatite-to-crustally-derived granite connection in thickened orogens. *Earth Sci. Rev.* 36, 83–130.

Brown M. 2007: Crustal melting and melt extraction, ascent and emplacement in orogens: mechanisms and consequences. *J. Geol Soc. London* 164, 709–730.

Brown M. 2013: Granite: from genesis to emplacement. *Geol. Soc. Am. Bulletin* 125, 1079–1113.

Bucher K. & Grapes R. 2011: Petrogenesis of Metamorphic Rocks. *Springer-Verlag*, 1–428.

Carvalho B.B., Sawyer E.W. & Janasi V.A. 2016: Crustal reworking in a shear zone: transformation of metagranite to migmatite. *J. Metamorph. Geol.* 34, 237–264.

Champion D.C. & Smithies R.H. 2007: Geochemistry of Paleoarchean granites of the East Pilbara terrane, Pilbara craton, Western Australia: Implications for Early Archean crustal growth. *Develop Precambrian* Geol. 15, 369–409.

Chiu H-Y., Chung S-L., Zarrinkoub M.H., Mohammadi S.S., Khatib M.M. & Iizuka Y. 2013: Zircon U–Pb age constraints from Iran on the magmatic evolution related to Neotethyan subduction and Zagros orogeny. *Lithos* 162–163, 70–87.

Dasgupta S., Sengupta P., Guha D. & Fukuoka M. 1991: A refined garnet-biotite Fe-Mg exchange geothermometer and its application in amphibolites and granulites. *Contrib. Mineral. Petrol.* 109, 130–137.

Davoudian A.R., Genser J., Dachs E. & Shabanian N. 2008: Petrology of eclogites from north of Shahrekord, Sanandaj–Sirjan Zone, Iran. *Mineral. Petrol.* 92, 393–413.

Erdmann S., Jamieson R.A. & MacDonald M.A. 2009: Evaluating the Origin of Garnet, Cordierite, and Biotite in Granitic Rocks: a Case Study from the South Mountain Batholith, Nova Scotia. *J. Petrol.* 50, 1477–1503.

Fazlnia A.N. & Alizade A. 2013: Petrology and geochemistry of the Mamakan gabbroic intrusions, Urumieh (Urmia), Iran: Magmatic development of an intra-oceanic arc. *Periodico di Mineralogia* 82, 263–290.

Fazlnia A.N., Moradian A., Rezaei K., Moazzen M. & Alipour S. 2007: Synchronous Activity of Anorthositic and S-type Granitic magmas in Chah-Dozdan batholith, Neyriz, Iran: Evidence of Zircon SHRIMP and Monazite CHIME Dating. *J. Sci., I. R. Iran* 18, 221–237.

Fazlnia A.N., Schenk V., van der Straaten F. & Mirmohammadi M.S. 2009: Petrology, Geochemistry, and Geochronology of Trondhjemites from the Qori Complex, Neyriz, Iran. *Lithos* 112, 413–433.

Fazlnia A.N., Schenk V., Appel P. & Alizade A. 2013: Petrology, geochemistry, and geochronology of the Chah-Bazargan gabbroic intrusions in the south Sanandaj–Sirjan zone, Neyriz, Iran. *Inter. J. Earth Sci.* 102, 1403–1426.

Ferry J.M. & Spear F.S. 1978: Experimental calibration of the partitioning of Fe and Mg between biotite and garnet. *Contrib. Mineral. Petrol.* 66, 113–117.

García-Arias M. & Stevens G. 2017a: Phase equilibrium modelling of granite magma petrogenesis: A. An evaluation of the magma compositions produced by crystal entrainment in the source. *Lithos* 277, 131–153.

García-Arias M. & Stevens G. 2017b: Phase equilibrium modelling of granite magma petrogenesis: B. An evaluation of the magma compositions that result from fractional crystallization. *Lithos* 277, 109–130.

García-Arias M., Corretge L.G. & Castro A. 2012: Trace element behavior during partial melting of Iberian orthogneisses: An experimental study. *Chem. Geol*. 292–293, 1–17.

Gessmann C.K., Spiering B. & Raith M. 1997: Experimental study of the exchange between garnet and biotite: Constraints on the mixing behavior and analysis of the cation-exchange mechanisms. *Am. Mineral.* 82, 1225–1240.

Golonka J. 2004: Plate tectonic evolution of the southern margin of Eurasia in the Mesozoic and Cenozoic. *Tectonophysics* 381, 235–273.

Harris N., Ayres M. & Massey J. 1995: Geochemistry of granitic melts produced during the incongruent melting of muscovite-implications for the extraction of Himalayan leucogranite magmas. *J. Geophys. Res.* 100, 15767–15777.

Harris N., McMillan M., Holness M., Uken R., Watkeys M., Rogers N. & Fallick A. 2003: Melt generation and fluid flow in the thermal aureole of the Bushveld Complex. *J. Petrol.* 44, 1031–1054.

Hassanzadeh J. & Wernicke B.P. 2016: The Neotethyan Sanandaj–Sirjan zone of Iran as an archetype for passive margin-arc transitions. *Tectonics* 35, 586–621.

Healy B., Collins W.J. & Richards S.W. 2004: A hybrid origin for Lachlan S-type granites: the Murrumbidgee Batholith example. *Lithos* 78, 197–216.

Henry D.J. & Guidotti C.V. 2002: Titanium in biotite from metapelitic rocks: Temperature effects, crystal-chemical controls, and petrologic applications. *Am. Mineral*. 87, 375–382.

Hodges K.V. & Spear F.S. 1982: Geothermometry, geobarometry and the Al_2SiO_5 triple point at Mt. Moosilauke, New Hampshire. *Am. Mineral.* 67, 1118–1134.

Holdway M.J. & Lee S.M. 1977: Fe-Mg cordierite stability in high-grade pelitic rocks based on experimental, theoretical and natural observations. *Contrib. Mineral. Petrol.* 63, 175–198.

Holtz F. & Johannes W. 1994: Maximum and minimum water contents of granitic melts; implications for chemical and physical properties of ascending magmas. *Lithos* 32, 149–159.

Jamshidi F. 2003: Petrology and petrogenesis study on the Chah-Dozdan granitoids, southeast ShahrBabak. *M.Sc. Thesis*, *Kerman University of Shahid-Bahonar*, Iran, 1–214 (in Persian).

Kaneko Y. & Miyano T. 2004: Recalibration of mutually consistent garnet-biotite and garnet-cordierite geothermometers. *Lithos* 73, 255–269.

Karimi S., Tabatabaei Manesh S.M., Safaei H. & Sharifi M. 2012: Metamorphism and Deformation of Golpayegan Metapelitic Rocks, Sanandaj_Sirjan Zone, Iran. *Petrology* 20, 658–675.

Keskin M. 2002: FC–Modeler: a Microsoft® Excel© spreadsheet program for modeling Rayleigh fractionation vectors in closed magmatic systems. *Comput. Geosci.* 28, 919–928.

Khadivi S., Mouthereau F., Barbarand J., Adatte T. & Lacombe O. 2012: Constraints on paleodrainage evolution induced by uplift and exhumation on the southern flank of the Zagros–Iranian Plateau. *J. Geol. Soc. London* 169, 83–97.

Kretz R. 1983: Symbols for rock-forming minerals. *Am. Mineral.* 68, 277–279.

Kriegsman L.M. & Hensen B.J. 1998: Back reaction between restite and melt: implications for geothermobarometry and pressure–temperature paths. *Geology* 26, 1111–1114.

Kriegsman L.M. 2001: Partial melting, partial melt extraction and partial back reaction in anatectic migmatites. *Lithos* 56, 75–96.

Lavaure S. & Sawyer E.W. 2011: Source of biotite in the Wuluma Pluton: Replacement of ferromagnesian phases and disaggregation of enclaves and schlieren. *Lithos 125*, 757–780.

Li Y.H. 2000: A compendium of geochemistry: from Solar Nebula to the Human Brain. *Princeton University Press*, Princeton, 1–475.

Makrygina V.A. 1977: Role of metamorphic zonation in distribution of pegmatites and migmatites of different composition. *Inter. Geol. Rev.* 19, 1133–1141.

McQuarrie N., Stock J.M., Verdel C. & Wernicke B.P. 2003: Cenozoic evolution of Neotethys and implications for the causes of plate motions. *Geophys. Res. Lett.* 30, 2036–2039.

Mehnert K.R. 1968: Migmatites and the origin of granitic rocks. *Developments in Petrology* 1, *Elsevier*, Amsterdam, 1–393.

Mohajjel M. & Fergusson C.L. 2014: Jurassic to Cenozoic tectonics of the Zagros Orogen in northwestern Iran. *Inter. Geol. Rev.* 56, 263–287.

Mohajjel M., Fergusson C.L. & Sahandi M.R. 2003: Cretaceous–Tertiary convergence and continental collision, Sanandaj–Sirjan zone, Western Iran. *J. Asian Earth Sci.* 21, 397–412.

Molinaro M., Zeyen H. & Laurencin X. 2005: Lithospheric structure underneath the SE Zagros Mountains, Iran: recent slab breakoff? *Terra Nova* 25, 1–6.

Mouthereau F. 2011: Timing of uplift in the Zagros belt/Iranian plateau and accommodation of late Cenozoic Arabia/Eurasia convergence. In: Lacombe O. Grasemann B. & Simpson G. (Eds.): Geodynamic Evolution of the Zagros. *Geol. Mag.* 148, 726–738.

Mouthereau F., Lacombe O. & Vergés J. 2012: Building the Zagros collisional orogen: Timing, strain distribution and the dynamics of Arabia/Eurasia plate convergence: *Tectonophysics* 532–535, 27–60.

Moyen J.-F., Laurent O., Chelle-Michou C., Couzinié S., Vanderhaeghe O. Zeh A. Villaros A. & Gardien V. 2017: Collision vs. subduction-related magmatism: Two contrasting ways of granite formation and implications for crustal growth. *Lithos* 277, 154–177.

Nabelek P.I. & Bartlett C. 2000: Fertility of metapelites and metagraywackes during leucogranite generation: An example from the Black Hills, USA. *Trans. Royal Soc. Edinburgh: Earth Sci.* 91, 1–14.

Nash W.P. & Crecraft H.R. 1985: Partition coefficients for trace elements in silicic magmas. *Geochim. Cosmochim. Acta* 49, 2309–2322.

Omrani J., Agard P., Whitechurch H., Benoit M., Prouteau G. & Jolivet L. 2008: Arc-magmatism and subduction history beneath the Zagros Mountains, Iran: A new report of adakites and geodynamic consequences. *Lithos* 106, 380–398.

Patiño Douce A.E. 1999: What do experiments tell us about the relative contributions of crust and mantle to the origin of granitic magmas? In: Castro A. Fernandez C. & Vigneressese J.L. (Eds.): Understanding Granites: Intergrating New and Classical Techniques. *Geol. Soc. London* 168, 55–75.

Patiño Douce A.E. & Harris N. 1998: Experimental constraints on Himalayan anatexis. *J. Petrol.* 39, 689–710.

Perchuk L.L. & Lavrent'eva I.V. 1983: Experimental investigation of exchange equilibria in the system cordierite-garnet-biotite. In: Saxena S.K. (Ed.): Kinetics and equilibrium in mineral reactions. *Springer-Verlag, Berlin, Adv. Phys. Geoch.* 3, 199–240.

Raymond L.A. 2007: Petrology: the study of igneous, sedimentary and metamorphic rocks. *McGraw-Hill*, New York, 1–720.

Ricou L.E. 1994: Tethys reconstructed: Plates, continental fragments and their boundaries since 260 Ma from Central America to South-eastern Asia. *Geodinamica Acta* 7, 169–218.

Robinson P. 1991: The eye of the petrographer, the mind of the petrologist. *Am. Mineral.* 76, 1781–1810.

Sabzehei M., Navazi M., Ghavidel M. & Hamdi S.B. 1992: Geological map of Neyriz (Scale 1:250,000). *Geological Survey of Iran*.

Saki A., Moazzen M. & Baharifar A.A. 2012: Migmatite microstructures and partial melting of Hamadan metapelitic rocks, Alvand contact aureole, western Iran. *Inter. Geol. Rev.* 54, 1229–1240.

Sarkarinejad K., Godin L. & Faghih A. 2009: Kinematic vorticity flow analysis and $^{40}Ar/^{39}Ar$ geochronology related to inclined extrusion of the HP–LT metamorphic rocks along the Zagros accretionary prism, Iran. *J. Struct. Geol.* 1, 691–706.

Sawyer E.W. 1991: Disequilibrium melting and the rate of meltresiduum separation during migmatitization of mafic rocks from the Grenville Front, Quebec. *J. Petrol.* 32, 701–738.

Sawyer E.W. 1996: Melt segregation and magma flow in migmatites: implications for the generation of granite magmas. *Transactions of the Royal Society of Edinburg, Earth Sci.* 87, 85–94.

Sawyer E.W. 2008a: Atlas of migmatites. *NRC Research Press, Canadian Mineralogist, Spec. publ.*, 1–371.

Sawyer E.W. 2008b: Working with Migmatites: Nomenclature for the Constituent Parts. In: Sawyer E.W. (Eds.): Working with Migmatites. *Mineral. Assoc. Can., Short Course Series* 38, 1–28.

Sawyer E.W. 2014: The inception and growth of leucosomes: microstructure at the start of melt segregation in migmatites. *J. Metamorph. Geol*. 32, 695–712.

Shafaii Moghadam H., Ghorbani G., Zaki Khedr M., Fazlnia N., Chiaradia M., Eyuboglu Y., Santosh M., Galindo Francisco C., Lopez Martinez M., Gourgaud A. & Arai S. 2014: Late Miocene K-rich volcanism in the Eslamieh Peninsula (Saray), NW Iran: Implications for geodynamic evolution of the Turkish–Iranian High Plateau. *Gondwana Res.* 26, 1028–1050.

Shaw D.M. 1970: Trace element fractionation during anatexis. *Geochim. Cosmochim. Acta* 34, 237–243.

Sheikholeslami M.R. 2015: Deformations of Palaeozoic and Mesozoic rocks in southern Sirjan, Sanandaj–Sirjan Zone, Iran. *J. Asian Earth Sci.* 106, 130–149.

Sheikholeslami R., Bellon H., Emami H., Sabzehei M. & Pique I. 2003: Nouvellés donneés structurales et datatious $^{40}K–^{40}Ar$ sur roches metamorphiques de lá region de Neyriz (Zone de Sanandaj–Sirjan, Iran meridional): Leur tethysien du Moyen-Orient. *Compt. Rend. Geosci.* 335, 981–991.

Sheikholeslami M.R., Pique A., Mobayen P., Sabzehei M., Bellon H., & Emami H. 2008: Tectono-metamorphic evolution of the Neyriz metamorphic complex, Quri-Kor-e-Sefid area (Sanandaj–Sirjan Zone, SW Iran). *J. Asian Earth Sci.* 31, 504–521.

Sheppard S., Occhipinti S.A. & Tyler I.M. 2003: The relationship between tectonism and composition of granitoid magmas, Yarlarweelor Gneiss Complex, Western Australia. *Lithos* 66, 133–154.

Sisson T.W. & Bacon C.R. 1992: Garnet/high-silica rhyolite trace-element partition coefficients measured by ion microprobe. *Geochim. Cosmochim. Acta* 56, 2133–2136.

Spear F.S. 1993: Metamorphic phase equilibria and pressure–temperature-time paths. *Mineral. Soc. Am.*, New York, 1–799.

Stevens G., Villaros A. & Moyen J.F. 2007: Selective peritectic garnet entrainment as the origin of geochemical diversity in S-type granites. *Geology* 35, 9–12.

Taylor J. & Stevens G. 2010: Selective entrainment of peritectic garnet into S-type granitic magmas: Evidence from Archaean mid-crustal anatectites. *Lithos* 120, 277–292.

Taylor S.R. & McLennan S.M. 1985: The Continental Crust: its composition and evolution. *Blackwell Scientific Publishers*, Oxford, 1–312.

Thompson P.H. 1976: Isograd patterns and pressure-temperature distributions during regional metamorphism. *Contrib. Mineral. Petrol.* 57, 277–295.

Villaros A. Stevens G. Moyen J.-F. & Buick I.S. 2009: The trace element compositions of S-type granites: evidence for disequilibrium melting and accessory phase entrainment in the source. *Contrib. Mineral. Petrol*. 158, 543–561.

Watson E.B. & Harrison T.M. 1983: Zircon saturation revisited: temperature and composition effects in a variety of crustal magma types. *Earth Planet. Sci. Lett.* 64, 295–304.

White R.W. & Powell R. 2002: Melt loss and the preservation of granulite facies mineral assemblages. *J. Metamorph. Geol.* 20, 621–632.

Wu C., Zhang J. & Ren L. 2004: Empirical garnet–biotite–plagioclase–quartz (GBPQ) geobarometry in medium- to high-grade metapelites. *J. Petrol.* 45, 1907–1921.

Yakymchuk C. & Brown M. 2014: Consequences of open-system melting in tectonics. *J. Geol Soc., London* 171, 21–40.

Yousefirad M. 2011: Genetic relation of the Zagros thrust and Sanandaj–Sirjan zone. *J. Am. Sci.* 7, 835–841.

Supplementum

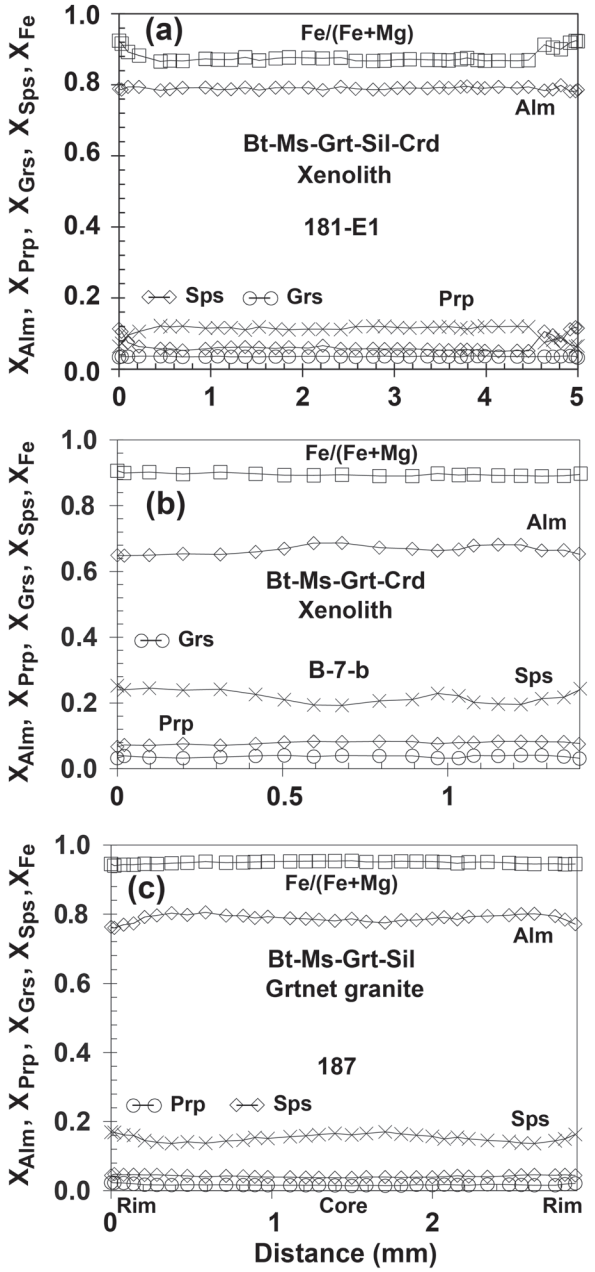

Fig. S1. Chemical compositions of garnet grains of metapelitic xenoliths and peraluminous granites. **a** — Migmatitic xenolith; **b** — Metapelitic xenolith without bands, pods and patches of leucocratic quartzo-feldspathic melt (leucosome); **c** — peraluminous granite patch in the Chah-Bazargan batholith.

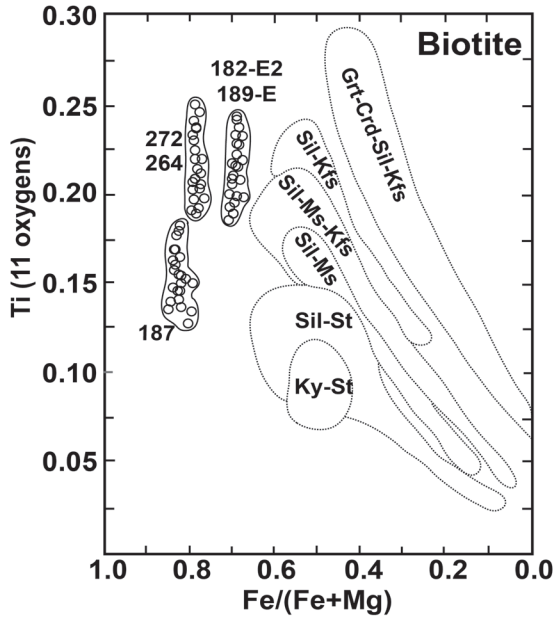

Fig. S2. Discriminating diagram of biotite. Plot of Ti (per 11 oxygens) as a function of Fe/(Fe+Mg) for biotite grains (Robinson 1991) from different rock types. Number 187 is garnet-bearing peraluminous granite. Numbers 264 and 272 are cordierite-bearing peraluminous granite. Numbers 182-E2 and 189-E are migmatitic xenoliths.

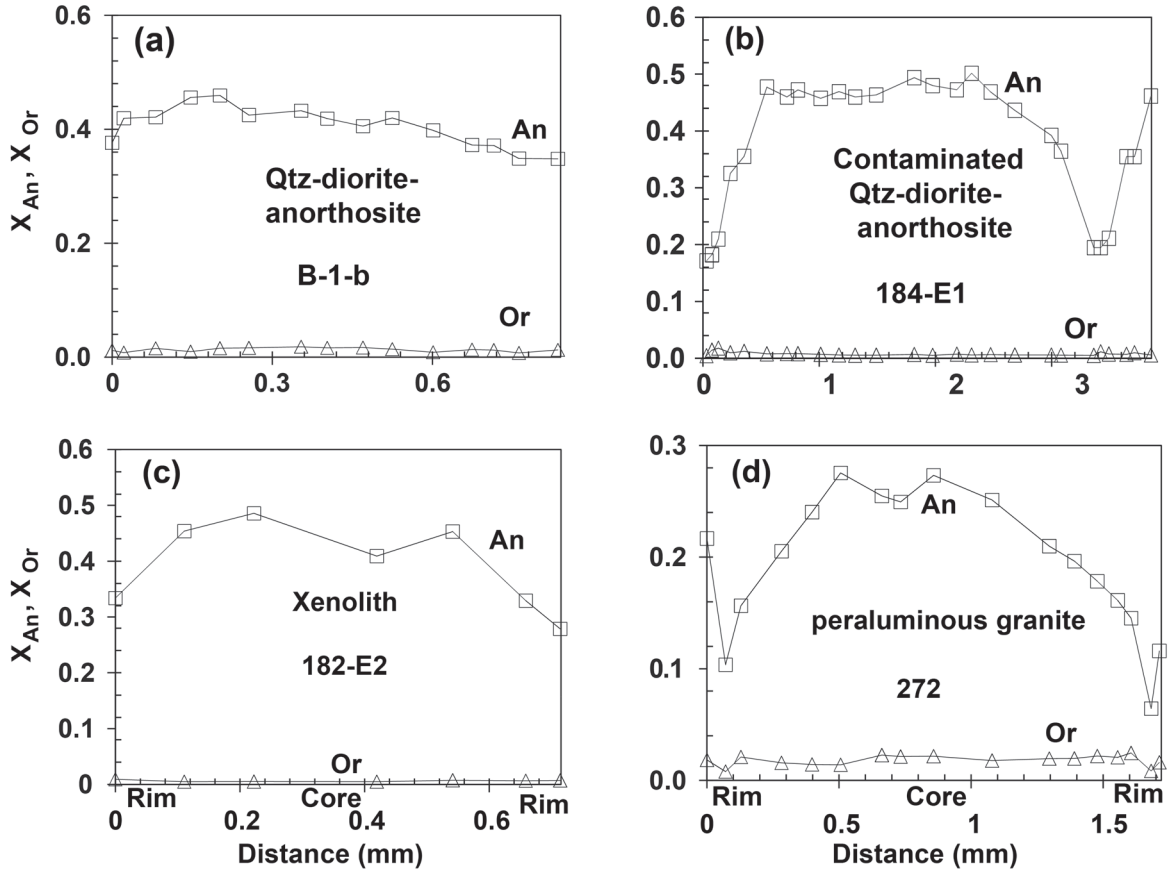

Fig. S3. Chemical composition of different rock types plagioclase. **a** — Quartz-diorite (Chah-Bazargan batholith); **b** — Contaminated quartz-diorite. This picture suggests that magma mixing has occurred between quartz dioritic and peraluminous granitic melts; **c** — Migmatitic xenolith; **d** — Peraluminous granite. Core of the grain is presumably a relic of the quartz-diorite and rim has been crystallized from the peraluminous granitic melt. Outer rim of the grain suggests that magma mixing has occurred between quartz dioritic and peraluminous granitic melts.

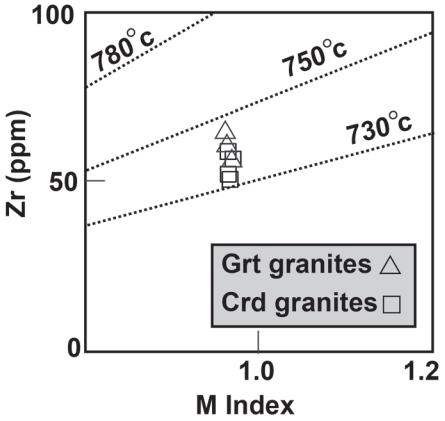

Fig. S4. Zirconium contents against M index defined as cation ratio (Na+K+2Ca)/(Al*Si) for the peraluminous granite of the Chah-Bazargan batholith. Lines indicate zirconium saturation isotherms calculated following Watson & Harrison (1983).

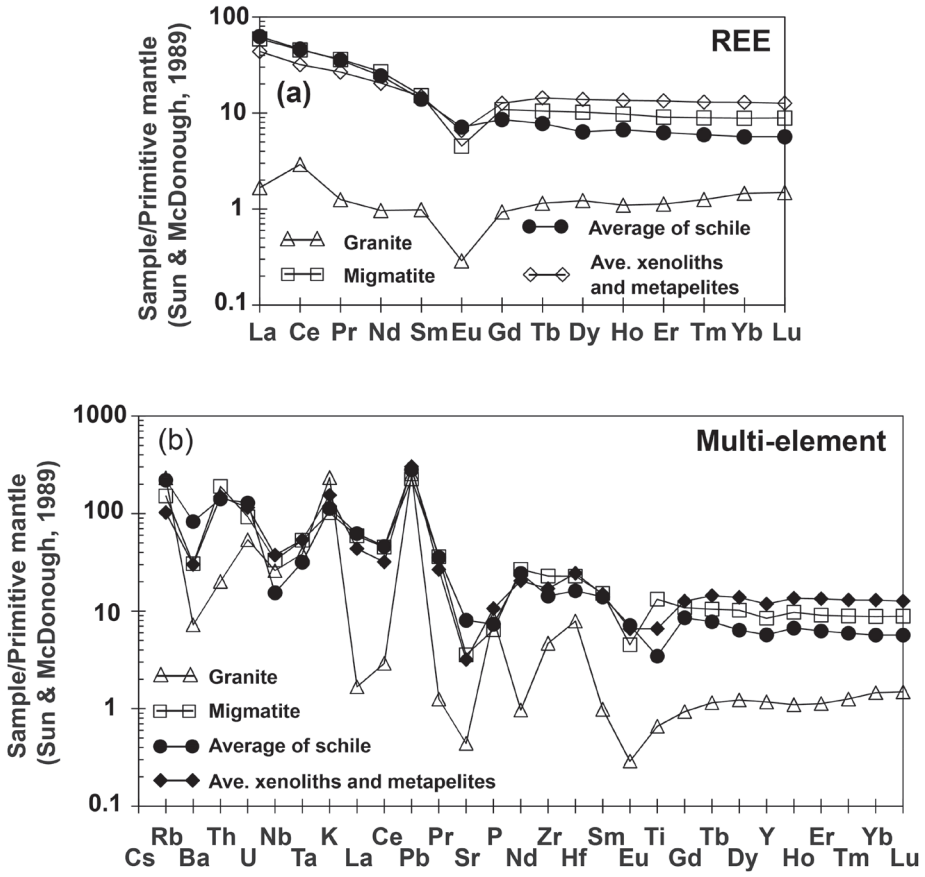

Fig. S5. Continental crust normalized REE and multi-element plots for averages of samples of Chah-Bazargan batholith. **a** — Normalized REE diagram; **b** — Normalized multi-element diagram. Normalization values after Taylor & McLennan (1985).

Table S1: Mineralogy and detailed mineral assemblage of all rock types of Chah-Bazargan, Talle-Pahlevani gabbroic intrusions and Qori Barrovian-type metamorphic complex.

	Minerals	
Rock type	**Metapelites**	**Metabasites**
Qori Barrovian-type metamorphic complex (QMC)	Biotite+Garnet+Kyanite+Plagioclase+ K-felspare+Quartz+Opaque minerals	Hornblande+Garnet+ Plasioclase+Quartz+ Biotite+Titanite
Rock type	**Chah-Bazargan intrusions**	**Talle-Pahlevani intrusions**
Chah-Bazargan quartz-dioritic and Talle-Pahlevani gabbroic intrusions	Plagioclase, Quartz, Clinopyroxene, Titanite, Opaque minerals	Plagioclase, Olivine, Clinopyroxene, Hornblande, Biotite, Titanite, Opaque minerals
Rock type	**Peraluminous granites**	**Migmatitic xenoliths**
Chah-Bazargan migmatitic xenoliths and peraluminous granitic patches	Biotite, Muscovite, Plagioclase, K-felspare, Quartz, Cordierite, Opaque minerals, Sillimanite, Tourmaline	Biotite+Plagioclase+K-felspare+Quartz+ Cordierite+Garnet+Opaque minerals+ Sillimanite
	Biotite, Muscovite, Plagioclase, K-felspare, Quartz, Opaque minerals, Garnet, Sillimanite, Tourmaline, ±Cordierite,	Biotite+Plagioclase+K-felspare+Quartz+ Cordierite+Opaque minerals+ Sillimanite+Spinel±Garnet

Table S2: Detailed petrographic observations of all rock types in the Chah-Bazargan intrusion.

Mineral phase			Qtz	Pl	Chl	Bt	Ms	Grt	Ky	Sil	And	Crd	Kf	Mc	Hbl	Cpx	Tou	Zr	Ap	Ilm	Ore
Sample	**Enclave**																				
AF-180-E1	N 29 42 07	E 54 37 08	X	X	S	X	X					X						A I	A I		X
AF-180-E2	29 42 07	54 37 08	X	X		X	X					X						A I	A I		X
AF-180-E3	29 42 07	54 37 08	X	X		X	X					X						A I	A I		X
AF-180-E4	29 42 07	54 37 08	X	X	S	X	X					X						A I	A I		X
AF-181-E2	29 30 17	54 37 33	X	X		X	X	X										A I	A I	A	X S
AF-181-E4	29 30 17	54 37 33	X	X	S	X I	X I					X	X				A	A I	A I		X I
AF-182-E1	29 38 45	54 38 51	X	X		X	X	X										A I	A I		X
AF-182-E2	29 38 45	54 38 51	X	X	S	X	X I					X	A					A I	A I		X S I
AF-184-E1	29 38 15	54 40 53	X	X		X	A											A I	A I		A S I
AF-184-E2	29 38 15	54 40 53	X	X		X	A											A I	A I		A I
AF-185-E1	29 38 14	54 44 05	X	X		X	X			A	X		X				A	A I	A I		A
AF-185-E2	29 38 14	54 44 05	X	X	S	X	X	A		A	A	A	X				A	A I	A I	A	X I
AF-185-E3	29 38 14	54 44 05	X	X	S	X	X			A	A		X				A	A I	A I		X I
AF-188-E1	29 38 49	54 39 01	X	X		X		A I		A	A	X	A				A	A I	A I		A
AF-188-E2	29 38 49	54 39 01	X	X	S	X	X	X		A		X	A					A I	A I	A	A
AF-188-E3	29 38 49	54 39 01	X	X	S	X												A I	A I		A
AF-188-E3	**Xenocryst in enclave**						X		X												
AF-188-E4	29 38 49	54 39 01	X	X	S	X	X					X						A I	A I		X
AF-189-E1	29 38 46	54 39 03	X	X		A	A						X	X			A		A I		
AF-191-E	29 42 50	54 42 07	X	X		X	A	X										A I	A I		X
AF-B-7-a	29 42 29	54 44 16	X	X		X I	X I											A I	A I		X I
AF-B-7-b	29 42 29	54 44 16	X	A	S	A	A	X I		A	A	X	A	A				A I	A I		A
AF-B-7-c	29 42 29	54 44 16	X	X		X	X	X										A I	A I		X
AF-B-10	29 41 55	54 43 27	X	X		X	X	A I		A								A I	A I		A I
AF-B-7-e	29 42 29	54 44 16	X	X		X		X										A I	A I		X
AF-269-f	29 38 43	54 39 07	X	A	S	X	X	A			X							A I	A I		A S
AF-B-7	29 42 29	54 44 16	X	X		X		X										A I	A I		X
AF-B-4	**Uneqilibrium enclave**		X	X		X									A	A	A	A I	A I		A
	29 42 08	54 45 23																			
AF-6	**Dioritic enclave**			X	S											X			A I		A
	29 42 14	54 42 59																			
	Chah-Bazargan intrusion																				
AF-B-8-a	29 42 27	54 44 14	X	X	S	X	X						X					A I	A I		
AF-B-1-b	29 42 11	54 45 33	X	X									X					A			
AF-269-a	29 40 14	54 38 48	X	A	S	X	X	X			A										
AF-265	29 39 46	54 39 17	X	X		X	X											A I	A I		A S
AF-269-c	29 38 43	54 39 06	X	A	S	X I	X I				X							A I	A I		A S
AF-269-e	29 38 43	54 39 06	X	A	S	X	X				X							A I	A I		X S
AF-271	29 38 47	54 38 25	X I	A	S	X I	X I	X										A I	A I		X S
AF-194-d	29 39 38	54 42 26	X		S	A									X			A I	A I		A S
	Peraluminous granite from Chah-Bazargan intrusion																				
AF-140-1	29 42 18	54 39 47	X	X		A	X	X		I	A I	A I	X	X			A I	A I	A I	A I	
AF-187	29 41 08	54 41 04	X	X		X	X	X			A I	A I	X	X			A I	A I	A I	A I	
AF-190-B	29 42 49	54 42 08	X	X		A	X	X		I	A I	A I	X	X			A I	A I	A I	A I	
AF-189-E	29 38 46	54 39 03	X	X		X	X	X		I	A I	A I	X	X			A I	A I	A I	A I	
AF-260	29 39 49	54 39 21	X	X		X	X				A I	X	X	X			A I	A I	A I	A I	
AF-264	29 39 50	54 38 14	X	X		X	X			I	A I	X	X	X			A I	A I	A I	A I	
AF-272	29 38 48	54 38 26	X	X		X	X				A I	X	X	X			A I	A I	A I	A I	

Mineral Abbreviations: are from Kretz 1983.

Marked Abbreviations are: A — accessory and minor phase in matrix phase, I — inclusion in one mineral, R — relict phase, S — secondary phase, X — matrix phase.

Table S3: Chemical compositions of plagioclase, biotite, muscovite, garnet, K-feldspar, cordierite and spinel. **Notes:** Granite: Per-aluminous granite; Xeno: xenolith; Inn R: Inner rim; Out R: Outer rim; Anor: anorthosite; Cont: contaminated leuco-quartz diorite-anorthosite; Mat: matrix

Sample	269-f	269-f	B-7-b	B-7-b	272	272	272	273	273	B-1-b	B-1-b
Mineral	Pl	Pl	Pl	Pl	Pl	Pl	Pl	Pl	Pl	Pl	Pl
Type of rock	Xeno Rim	Xeno Core	Xeno Rim	Xeno Core	Granite Out r	Granite Inn r	Granite Core	Cont Rim	Cont Core	Anor Rim	Anor Core
SiO_2	64.56	59.74	59.56	55.09	62.49	66.33	61.17	63.65	56.42	58.33	55.96
Al_2O_3	22.66	25.90	25.63	28.37	23.42	20.43	24.09	23.25	28.47	25.92	27.32
Fe_2O_3	0.09	0.09	0.17	0.04	0.04	0.00	0.00	0.18	0.00	0.11	0.06
CaO	3.11	6.75	6.37	9.83	4.50	1.36	5.76	3.99	9.83	7.78	10.01
Na_2O	9.72	7.54	7.72	5.82	8.78	10.82	8.23	9.46	5.96	6.99	5.79
K_2O	0.08	0.08	0.17	0.09	0.32	0.15	0.25	0.18	0.12	0.20	0.12
BaO	0.03	0.02	0.04	0.00	0.00	0.01	0.05	0.02	0.02	0.00	0.00
Total	100.25	100.13	99.66	99.24	99.55	99.10	99.55	100.73	100.82	99.33	99.25
Si	2.84	2.66	2.66	2.50	2.78	2.94	2.73	2.80	2.51	2.62	2.53
Al^{IV}	1.17	1.36	1.35	1.52	1.23	1.07	1.27	1.20	1.50	1.37	1.46
Total	4.01	4.01	4.01	4.01	4.01	4.00	4.00	4.00	4.01	4.00	3.99
Fe^{3+}	0.00	0.00	0.01	0.00	0.00	0.00	0.00	0.01	0.00	0.00	0.00
Ca	0.15	0.32	0.31	0.48	0.21	0.06	0.28	0.19	0.47	0.38	0.49
Na	0.83	0.65	0.67	0.51	0.76	0.93	0.71	0.81	0.52	0.61	0.51
K	0.00	0.00	0.01	0.01	0.02	0.01	0.01	0.01	0.01	0.01	0.01
Ba	0.00	0.00	0.00	0.00	0.00	0.00	0.00	0.00	0.00	0.00	0.00
Total	0.98	0.98	0.99	0.99	0.99	1.00	1.00	1.01	0.99	1.00	1.00
An	0.15	0.33	0.31	0.48	0.22	0.06	0.28	0.19	0.47	0.38	0.48
Ab	0.85	0.67	0.68	0.51	0.77	0.93	0.71	0.80	0.52	0.61	0.51
Kfs	0.00	0.00	0.01	0.01	0.02	0.01	0.01	0.01	0.01	0.01	0.01

Sample	269-f	B-7-b	182-E2	269-f	B-7-b
Mineral	Bt	Bt	Bt	Ms	Ms
Type of rock	Xeno Mat	Xeno Mat	Xeno Mat	Xeno Mat	Xeno Mat
SiO_2	34.61	35.03	34.18	46.22	45.23
TiO_2	1.96	2.93	3.03	0.43	0.41
Al_2O_3	19.62	19.41	19.80	36.21	35.83
FeO	22.05	20.43	23.57	0.76	0.92
MgO	7.35	7.14	6.49	0.42	0.55
MnO	0.12	0.34	0.19	0.03	0.00
Na_2O	0.11	0.18	0.10	1.22	0.71
K_2O	9.36	9.74	9.65	9.86	11.09
Total	95.18	95.19	97.00	95.15	94.74
Si	5.35	5.38	5.23	6.13	6.08
Al^{IV}	2.66	2.62	2.77	1.87	1.92
Al^{VI}	0.92	0.90	0.81	3.79	3.75
Ti	0.23	0.34	0.35	0.04	0.04
Fe^{2+}	2.85	2.63	3.02	0.08	0.10
Mg	1.69	1.64	1.48	0.08	0.11
Mn	0.02	0.04	0.02	0.00	0.00
Na	0.03	0.05	0.03	0.31	0.18
K	1.85	1.91	1.88	1.67	1.90
Total	15.58	15.50	15.59	13.99	14.09
X_{Fe}	0.63	0.62	0.67	0.50	0.49

Sample	269-f	269-f	B-7-b	B-7-b	182-E2
Mineral	Grt	Grt	Grt	Grt	Grt
Type of rock	Xeno Rim	Xeno Core	Xeno Rim	Xeno Core	Xeno Rim
SiO_2	37.21	37.12	36.41	36.49	37.55
TiO_2	0.03	0.03	0.01	0.03	0.04
Al_2O_3	21.00	20.92	20.99	21.18	21.08
FeO	33.68	36.72	28.35	29.97	35.33
MgO	2.26	2.67	1.64	2.03	3.02
MnO	5.34	1.85	10.89	8.36	2.53
CaO	1.02	0.90	1.09	1.26	1.28
Total	100.54	100.22	99.38	99.33	100.83
Structural formulae on a basis of 12 oxygens					
Si	3.00	3.00	2.98	2.98	3.00
Al	2.00	1.99	2.03	2.04	1.99
Ti	0.00	0.00	0.00	0.00	0.00
Fe^{2+}	2.27	2.48	1.94	2.05	2.36
Mg	0.27	0.32	0.20	0.25	0.36
Mn	0.37	0.13	0.76	0.58	0.17
Ca	0.09	0.08	0.10	0.11	0.11
Total	8.00	8.00	8.00	8.00	8.00
Alm	0.76	0.83	0.65	0.69	0.79
Prp	0.09	0.11	0.07	0.08	0.12
Sps	0.12	0.04	0.25	0.19	0.06
Grs	0.03	0.03	0.03	0.04	0.04
X_{Fe}	0.89	0.89	0.91	0.89	0.87

Sample	187	264	272	182-E2
Mineral	Kfs	Kfs	Kfs	Kfs
Type of rock	Granite	Granite	Granite	Xeno
SiO_2	64.94	65.18	64.98	64.57
Al_2O_3	19.26	18.87	18.48	18.98
Fe_2O_3	0.07	0.00	0.05	0.05
CaO	0.05	0.00	0.04	0.02
Na_2O	1.78	1.67	1.50	1.37
K_2O	14.48	15.09	14.91	15.11
BaO	0.22	0.04	0.04	0.37
Total	100.81	100.85	100.01	100.46
Structural formulae on a basis of 8 oxygens				
Si	2.97	2.98	2.99	2.97
Al^{IV}	1.04	1.02	1.00	1.03
Total	4.00	4.00	4.00	4.00
Fe^{3+}	0.00	0.00	0.00	0.00
Ca	0.00	0.00	0.00	0.00
Na	0.16	0.15	0.13	0.12
K	0.84	0.88	0.88	0.89
Ba	0.00	0.00	0.00	0.01
Total	1.01	1.03	1.01	5.02
An	0.00	0.00	0.00	0.00
Ab	0.16	0.14	0.13	0.12
Kfs	0.84	0.86	0.87	0.88

Table S3 continuation: Chemical compositions of plagioclase, biotite, muscovite, garnet, K-feldspar, cordierite and spinel. **Notes:** Granite: Per-aluminous granite; Xeno: xenolith; Inn R: Inner rim; Out R: Outer rim; Anor: anorthosite; Cont: contaminated leuco-quartz diorite-anorthosite; Mat: matrix

Sample	**181-E**	**182-E2**	**264**
Mineral	**Crd**	**Crd**	**Crd**
Type of rock	**Xeno**	**Xeno**	**Granite**
SiO_2	48.31	48.18	48.21
TiO_2	0.00	0.00	0.00
Al_2O_3	33.05	33.12	33.16
FeO	10.39	11.92	11.89
MgO	6.36	6.08	5.97
MnO	0.31	0.36	0.36
CaO	0.02	0.03	0.00
Na_2O	0.34	0.13	0.15
K_2O	0.00	0.00	0.01
Total	98.77	99.82	99.75
	basis of 18 oxygens		
Si	5.00	4.97	4.98
Al^{IV}	1.00	1.03	1.02
Al^{VI}	3.04	3.00	3.01
Ti	0.00	0.00	0.00
Total	3.04	3.00	3.01
Fe^{2+}	0.90	1.03	1.03
Mg	0.98	0.94	0.92
Mn	0.03	0.03	0.03
Total	1.91	2.00	1.98
Ca	0.00	0.00	0.00
Na	0.07	0.03	0.03
K	0.00	0.00	0.00
Total	0.07	0.03	0.03
X_{Fe}	0.48	0.52	0.53

Sample	**182-E2**	**182-E2**	**187**
Mineral	**Spl**	**Spl**	**Spl**
Type of rock	**Xeno**	**Xeno**	**Granite**
SiO_2	0.05	0.05	0.01
TiO_2	0.02	0.02	0.01
Al_2O_3	58.34	58.77	59.34
Cr_2O_3	0.40	0.35	0.12
Fe_2O_3	1.34	0.58	0.02
FeO	35.81	35.49	35.73
MgO	1.64	1.93	2.12
MnO	0.44	0.39	0.25
ZnO	3.28	3.02	2.45
Total	101.30	100.60	100.06
	basis of 32 oxygens		
Si	0.01	0.01	0.00
Ti	0.00	0.00	0.00
Al^{IV}	15.67	15.81	15.97
Cr	0.07	0.06	0.02
Fe^{3+}	0.23	0.10	0.00
Total	15.99	15.99	16.00
Fe^{2+}	6.82	6.77	6.82
Mg	0.56	0.66	0.72
Mn	0.08	0.08	0.05
Zn	0.55	0.51	0.41
Total	8.01	8.01	8.00
X_{Fe}	0.93	0.91	0.90
X_{Cr}	0.00	0.00	0.00

Table S4: Temperatures estimated from different thermometers. Abbreviations are: B92-HW and B92-GS: Bhattacharya et al. (1992); Dasg91: Dasgupta et al. (1991); FS78: Ferry & Spear (1978); HS82: Hodges & Spear (1982); PL83: Perchuk & Lavrent'eva (1983); T76: Thompson (1976); HL77: Holdway & Lee (1977); GS97: Gessmann et al. (1997); KM04-Bt-Grt and KM04-Crd-Grt: Kaneko & Miyano (2004).

Sample	**kbar**	**B92-HW**	**B92-GS**	**Dasg91**	**FS78**	**HS82**	**PL83**	**T76**	**HL77**	**GS97**	**KM04-Bt-Grt**	**KM04-Crd-Grt**
269-f	6	624	623	540	659	670	626	662	633	640	645	625
B-7-b	6	560	522	521	613	628	602	627	603	605	590	–
182-E2	6	706	701	658	827	842	705	782	734	785	780	745
269-f	5	623	622	535	655	666	624	654	629	636	643	620
B-7-b	5	559	521	516	609	624	600	619	599	601	588	–
182-E2	5	706	700	652	822	837	702	774	730	778	778	740
269-f	4	622	621	530	651	661	621	647	626	632	641	615
B-7-b	4	558	520	511	605	620	597	612	596	595	586	–
182-E2	4	705	699	646	817	833	698	765	726	773	786	735
269-f	3	622	620	525	647	657	618	639	622	628	639	610
B-7-b	3	558	519	507	601	616	594	605	592	590	584	–
182-E2	3	704	698	640	812	828	695	756	722	770	784	730
269-f	2	621	620	520	642	653	615	631	619	624	637	605
B-7-b	**2**	**557**	**518**	**502**	**597**	**612**	**591**	**597**	**589**	**585**	**582**	–
182-E2	**2**	**703**	**697**	**634**	**807**	**823**	**692**	**748**	**718**	**767**	**782**	**725**

Table S5: Pressures estimated from different barometers. Abbreviations are, HS82: Hodges & Spear (1982); WU04: Wu et al. (2004); Ave: average of pressure.

Sample	°C	HS82	WU04	Ave
269-f	~640	1.6	2.5	2.1
B-7-b	~590	1.4	1.9	1.7
182-E2	~760	4.5	5.0	4.8

Table S6: Geochemical averages for selected metapelites and xenoliths without migmatitic texture and migmatitic xenoliths from the Chah-Bazargan batholith listed in Table 2.

	Average of metapelites and xenoliths n=10 Table 2	Average of migmatitic xenoliths n=3 Table 2
Ba	210.27	214.13
Rb	65.21	96.25
Sr	67.10	75.24
U	2.42	1.94
Th	12.71	16.19
Nb	26.70	23.77
Zr	190.30	256.33
Y	53.82	38.45
La	30.02	40.65
Ce	56.65	80.54
Pr	7.37	9.98
Nd	27.67	36.35
Sm	6.62	6.74
Eu	1.10	0.76
Gd	7.53	6.49
Tb	1.56	1.13
Dy	10.20	7.54
Ho	2.22	1.60
Er	6.42	4.36
Tm	0.96	0.66
Yb	6.38	4.35
Lu	0.94	0.66
Cr	69.61	109.16
Ni	31.37	67.53
P	1007	611
Ti	8773	17647
V	101.97	196.88
Co	13.47	21.34
Hf	7.55	7.06
Ta	2.20	2.18
Pb	21.57	16.06

Table S7: Calculated bulk partition coefficients (Kd) with 1 %, 5 %, 10 %, 20 %, 30 %, 40 %, and 50 % partial melting for selected Chah-Bazargan migmatitic xenoliths.

Source Tables 1 and 2.							
Value	f 0.05 Kd	f 0.1 Kd	f 0.2 Kd	f 0.3 Kd	f 0.4 Kd	f 0.5 Kd	$f_{0.5}/f_{0.05}$
Ba	1.56	1.22	1.10	1.06	1.05	1.04	0.66
Rb	−0.18	−0.45	−1.63	−13.33	5.16	2.82	−15.35
Sr	−0.86	−12.33	2.18	1.56	1.37	1.28	−1.48
U	0.17	0.29	0.45	0.55	0.62	0.67	3.95
Th	−0.30	−0.87	−13.22	3.53	2.16	1.76	−5.80
Nb	0.29	0.45	0.62	0.71	0.76	0.80	2.78
Zr	−0.24	−0.63	−3.47	7.07	2.81	2.06	−8.56
Y	0.11	0.20	0.33	0.43	0.50	0.56	5.00
La	−0.24	−0.62	−3.26	7.76	2.88	2.10	−8.86
Ce	−0.20	−0.51	−2.07	71.09	3.87	2.46	−12.13
Pr	−0.24	−0.62	−3.22	7.91	2.90	2.10	−8.91
Nd	−0.26	−0.72	−5.16	4.90	2.48	1.91	−7.22
Sm	1.57	1.22	1.10	1.06	1.05	1.04	0.66
Eu	0.10	0.18	0.31	0.40	0.47	0.52	5.28
Gd	0.24	0.38	0.55	0.65	0.71	0.76	3.19
Tb	0.12	0.21	0.35	0.45	0.52	0.57	4.84
Dy	0.12	0.22	0.36	0.46	0.53	0.59	4.73
Ho	0.11	0.20	0.34	0.43	0.51	0.56	4.94
Er	0.10	0.17	0.30	0.39	0.46	0.51	5.38
Tm	0.10	0.18	0.30	0.40	0.47	0.52	5.30
Yb	0.10	0.18	0.30	0.39	0.46	0.52	5.34
Lu	0.10	0.19	0.32	0.41	0.48	0.54	5.15
Cr	−0.16	−0.38	−1.23	−4.81	10.63	3.63	−22.69
Ni	−0.10	−0.23	−0.60	−1.27	−2.95	−14.09	136.81
P	0.07	0.13	0.24	0.32	0.38	0.43	6.09
Ti	−0.11	−0.25	−0.66	−1.48	−3.89	−176.25	1596.25
V	−0.12	−0.26	−0.71	−1.65	−4.87	27.92	−241.25
Co	−0.16	−0.37	−1.18	−4.34	12.94	3.82	−24.37
Hf	0.42	0.59	0.74	0.81	0.85	0.88	2.09
Ta	0.84	0.91	0.95	0.97	0.98	0.98	1.17
Pb	0.13	0.23	0.37	0.47	0.54	0.59	4.66

Table S8: Calculated bulk partition coefficients (Kd) for each mineral based on partition coefficients (mineral/granitic peraluminous melt) after Nash & Crecraft (1985), Sisson & Bacon (1992), Bea et al. (1994), and Keskin' software (2002).

Element	Kd (Grt)	Kd (Bt-Ms)	Kd (Kfs)	Kd (Pl)	Kd (Crd)	Kd (Ap)	Kd (Zr)	Kd (Ilm)	D_1	D_2	Co	$C^s = D \times C^o/(f+D(1-f))$						
												f_2 0.01	f_2 0.05	f_2 0.10	f_2 0.20	f_2 0.30	f_2 0.40	f_2 0.50
La	0.001	0.06	1.01	4.61	0.06	456	1.30	7.1	11.4	5.9	30.02	−30.4	−31.9	−34.0	−39.2	−46.2	−56.4	−72.2
Ce	0.01	0.05	0.86	3.87	0.07	569	2.04	7.8	13.9	7.1	56.65	−57.3	−60.1	−63.9	−73.4	−86.1	−104.1	−131.8
Nd	0.4	0.08	0.51	2.56	0.09	855	3.35	7.6	20.4	10.2	27.67	−28.0	−29.3	−31.1	−35.5	−41.3	−49.4	−61.4
Sm	6.4	0.06	0.42	1.45	0.10	1105	3.79	6.9	26.6	13.0	6.62	−6.69	−6.99	−7.41	−8.43	−9.77	−11.62	−14.34
Eu	9.3	0.05	2.32	2.99	0.01	23.8	0.45	2.5	2.4	1.1	1.10	−1.13	−1.22	−1.36	−1.78	−2.56	−4.55	−20.68
Gd	3.7	0.10	0.60	2.05	0.29	2133	9.21	0.00	50.0	24.0	7.53	−7.61	−7.94	−8.41	−9.51	−10.95	−12.91	−15.72
Yb	140	0.12	0.64	0.82	1.77	2216	278	4.1	68.2	30.3	6.38	−6.45	−6.73	−7.11	−8.04	−9.24	−10.87	−13.20
Lu	47	0.2	0.96	1.32	4.43	2981	923	3.6	76.4	37.4	0.94	−0.95	−0.99	−1.04	−1.18	−1.35	−1.59	−1.93
Y	130	0.1	0.5	0.78	0.72	162	71.4	0.20	19.3	6.6	53.82	−54.5	−57.1	−60.8	−69.9	−82.3	−99.8	−127.0
Cr	4	42.3	1.15	0.31	0.92	0.00	119.0	3	15.8	16.9	69.61	−70.4	−73.5	−77.9	−88.3	−102.0	−120.8	−148.0
Nb	0.05	24.50	0.27	0.04	0.01	0.00	0.00	11.6	8.8	9.9	26.70	−27.0	−28.2	−30.0	−34.2	−39.9	−47.7	−59.4

Note: D_1 = 11.60 % Grt + 34.80 % Bt-Ms + 11.6 % Kfs + 13.9 % Pl + 23.2 % Crd + 2.3 % Ap + 0.1 % Zr + 2.3 % Ilm;

D_2 = 3.3 % Grt + 38 % Bt + 4.4 % Kfs + 9.8 % Pl + 38 % Crd + 1.1 % Ap + 0.1 % Zr + 5.3 % Ilm

Element	Kd (Grt)	Kd (Bt-Ms)	Kd (Kfs)	Kd (Pl)	Kd (Crd)	Kd (Ap)	Kd (Zr)	Kd (Ilm)	D_1	D_2	Co	$C^s = D \times C^o/(f+D(1-f))$						
												f_1 0.01	f_1 0.05	f_1 0.10	f_1 0.20	f_1 0.30	f_1 0.40	f_1 0.50
La	0.001	0.06	1.01	4.61	0.06	456	1.30	7.1	11.4	5.9	30.02	−30.4	−31.8	−33.7	−38.4	−44.6	−53.1	−65.8
Ce	0.01	0.05	0.86	3.87	0.07	569	2.04	7.8	13.9	7.1	56.65	−57.3	−59.9	−63.4	−72.1	−83.5	−99.2	−122.0
Nd	0.4	0.08	0.51	2.56	0.09	855	3.35	7.6	20.4	10.2	27.67	−28.0	−29.2	−30.9	−35.0	−40.4	−47.7	−58.2
Sm	6.4	0.06	0.42	1.45	0.10	1105	3.79	6.9	26.6	13.0	6.62	−6.68	−6.98	−7.38	−8.35	−9.60	−11.31	−13.75
Eu	9.3	0.05	2.32	2.99	0.01	23.8	0.45	2.5	2.4	1.1	1.10	−1.12	−1.19	−1.29	−1.54	−1.92	−2.55	−3.80
Gd	3.7	0.10	0.60	2.05	0.29	2133	9.21	0.00	50.0	24.0	7.53	−7.61	−7.94	−8.39	−9.46	−10.85	−12.72	−15.37
Yb	140	0.12	0.64	0.82	1.77	2216	278	4.1	68.2	30.3	6.38	−6.45	−6.72	−7.10	−8.00	−9.17	−10.74	−12.95
Lu	47	0.2	0.96	1.32	4.43	2981	923	3.6	76.4	37.4	0.94	−0.95	−0.99	−1.04	−1.18	−1.35	−1.58	−1.90
Y	130	0.1	0.5	0.78	0.72	162	71.4	0.20	19.3	6.6	53.82	−54.4	−56.8	−60.2	−68.2	−78.6	−92.9	−113.5
Cr	4	42.3	1.15	0.31	0.92	0.00	119.0	3	15.8	16.9	69.61	−70.4	−73.5	−77.9	−88.4	−102.2	−121.1	−148.6
Nb	0.05	24.50	0.27	0.04	0.01	0.00	0.00	11.6	8.8	9.9	26.70	−27.0	−28.3	−30.0	−34.3	−40.1	−48.1	−60.2

Note: D_1 = 11.60 % Grt + 34.80 % Bt-Ms + 11.6 % Kfs + 13.9 % Pl + 23.2 % Crd + 2.3 % Ap + 0.1 % Zr + 2.3 % Ilm;

D_2 = 3.3 % Grt + 38 % Bt + 4.4 % Kfs + 9.8 % Pl + 38 % Crd + 1.1 % Ap + 0.1 % Zr + 5.3 % Ilm